

# The primordial matter power spectrum on sub-galactic scales

Daniel Gilman<sup>1\*</sup>, Andrew Benson<sup>2</sup>, Jo Bovy<sup>1</sup>, Simon Birrer<sup>3,4</sup>, Tommaso Treu<sup>5</sup>, Anna Nierenberg<sup>6</sup>

<sup>1</sup>Department of Astronomy and Astrophysics, University of Toronto, 50 St. George Street, Toronto, ON, M5S 3H4, Canada

<sup>2</sup>Carnegie Observatories, 813 Santa Barbara Street, Pasadena, CA 91101, USA

<sup>3</sup>Kavli Institute for Particle Astrophysics and Cosmology and Department of Physics, Stanford University, Stanford, CA 94305, USA

<sup>4</sup>SLAC National Accelerator Laboratory, Menlo Park, CA, 94025

<sup>5</sup>Department of Physics and Astronomy, University of California, Los Angeles, CA 90095, USA

<sup>6</sup>Department of Physics, University of California Merced, 5200 North Lake Rd. Merced, CA 95343

Accepted . Received

## ABSTRACT

The primordial matter power spectrum quantifies fluctuations in the distribution of dark matter immediately following inflation. Over cosmic time, over-dense regions of the primordial density field grow and collapse into dark matter halos, whose abundance and density profiles retain memory of the initial conditions. By analyzing the image magnifications in eleven strongly-lensed and quadruply-imaged quasars, we infer the abundance and concentrations of low-mass halos, and cast the measurement in terms of the amplitude of the primordial matter power spectrum  $P(k)$  on (inverse) length scales  $1 < k < 50 \text{ Mpc}^{-1}$ . Assuming an analytic model for the power spectrum and accounting for several sources of potential systematic uncertainty, including three different models for the halo mass function, we infer  $\log_{10}(P/P_{\Lambda\text{CDM}})$ , the power spectrum amplitude relative to the predictions of the concordance cosmological model, of  $0.0_{-0.4}^{+0.4}$ ,  $0.1_{-0.7}^{+0.6}$ , and  $0.2_{-1.0}^{+0.9}$  at  $k = 10, 25$  and  $50 \text{ Mpc}^{-1}$  at 68% confidence. Our inference makes contact with the properties of the early Universe on smaller scales than existing measurements have accessed, and agrees with the predictions of cold dark matter and single-field slow-roll inflation.

**Key words:** [gravitational lensing: strong - cosmology: dark matter - cosmology: early Universe - cosmology: inflation]

## 1 INTRODUCTION

The theory of inflation, first proposed by Alan Guth in 1981 (Guth 1981), simultaneously resolved outstanding challenges to the ‘Big Bang’ paradigm while providing a predictive framework to characterize the initial conditions for structure formation. Soon after the original paper by Guth, several authors pointed out (Starobinsky 1982; Guth & Pi 1982; Bardeen et al. 1983) that fluctuations of a scalar field driving inflation, the ‘inflaton’, would seed inhomogeneities in the distribution of matter. The primordial matter power spectrum,  $P(k)$ , quantifies these inhomogeneities as a function of (inverse) length scale  $k$ . In addition to inflation, dark matter physics beyond the concordance model of cold dark matter plus a cosmological constant,  $\Lambda\text{CDM}$ , can alter the shape of the matter power spectrum on small scales (Bode et al. 2001; Schneider et al. 2012; Vogelsberger et al. 2016). The connection to the inflaton and dark matter physics

makes  $P(k)$  one of the most fundamental quantities in cosmology.

The largest scale constraints on  $P(k)$  come from analyses of the Cosmic Microwave Background (CMB) radiation (Planck Collaboration et al. 2020c,a,b), and the clustering an internal structure of massive galaxies (Fedeli et al. 2010; Reid et al. 2010; Troxel et al. 2018). Pushing to smaller scales, the Lyman- $\alpha$  forest uses the presence of neutral hydrogen as a proxy for the underlying dark matter density field, and delivers constraints on  $P(k)$  on scales reaching  $k \sim 5 \text{ Mpc}^{-1}$  (Viel et al. 2004; Chabanier et al. 2019). Recently, Sabti et al. (2021) used measurements of the ultra-violet luminosity function, which connects to  $P(k)$  through the abundance of galaxies at redshifts  $4 - 10$ , to push to even smaller scales, reaching  $k = 10 \text{ Mpc}^{-1}$ . In combination the data agree with the predictions of  $\Lambda\text{CDM}$ , and suggest a common origin for the density perturbations in the early

Universe described by power-law spectrum  $P(k) \sim k^{-n_s}$ , with the spectral index  $n_s = 0.9645 \pm 0.0044$  measured precisely from analyses of the CMB (Planck Collaboration et al. 2020c). The value of  $n_s$  inferred from the data amounts to a success for slow-roll inflation (Linde 1982; Albrecht & Steinhardt 1982), which predicts a value of  $n_s$  close to unity.

Constraints on the power spectrum on smaller length scales  $k > 10 \text{ Mpc}^{-1}$ , beyond the reach of existing measurements, could reveal departures from the form of  $P(k)$  that the CMB, Lyman- $\alpha$  forest, and other probes have so precisely measured. Deviation from the power-law form of  $P(k)$ , particularly a scale-dependence, or ‘running’, of the spectral index larger than  $|n_s - 1|$ , could falsify slow-roll inflation. Such a finding would have profound consequences for inflationary cosmology, and perhaps the nature of dark matter (Chluba et al. 2012). However, inferring  $P(k)$  on smaller scales becomes increasingly challenging because structure formation becomes highly non-linear, complicating the mapping between  $P(k)$  and observables. Physically, this non-linearity manifests in the formation of gravitationally-bound structures referred to as dark matter halos.

Strong gravitational lensing by galaxies provides a direct and elegant observational tool to determine the properties of otherwise-undetectable dark matter halos (Dalal & Kochanek 2002; Vegetti et al. 2014; Inoue et al. 2015; Hezaveh et al. 2016; Birrer et al. 2017; Gilman et al. 2020a; Hsueh et al. 2020). Strong lensing refers to the deflection of light by the gravitational field of a massive foreground object, with the result that a single background source becomes multiply-imaged. In quadruply-imaged quasars (quads), a galaxy and its host dark matter halo, which together we refer to as the ‘main deflector’, produce four highly magnified but unresolved images of a background quasar. The image magnifications in quads depend on second derivatives of the projected gravitational potential in the plane of the lens,  $\Phi$ , which depends on the projected mass density,  $\kappa$ , through the Poisson equation in two dimensions,  $\nabla^2\Phi \propto \kappa$ . A compact dark halo that dominates the local mass density near an image can impart a large perturbation to  $\nabla^2\Phi$ , and hence the image magnification, even if the halo has a mass orders of magnitude lower than the main deflector. Using existing datasets and analysis methods, lensing of compact, unresolved sources reveals the properties of halos with masses below  $10^8 M_\odot$ , with a minimum halo mass sensitivity around  $10^7 M_\odot$  (Gilman et al. 2019).

To identify the corresponding  $k$ -scales relevant for an inference of  $P(k)$ , we can compute the Lagrangian radius  $R_l$  for a halo of mass  $m$  defined by  $m = (4\pi/3)\Omega_m \rho_{\text{crit}} R_l^3$ , where  $\Omega_m \rho_{\text{crit}}$  represents the contribution to the critical density of the Universe from dark matter, and evaluate the corresponding wavenumber  $k = 2\pi/R_l$ . The minimum halo mass sensitivity of quad lenses depends on the size of the background source. Existing measurements of narrow-line flux ratios can reach  $10^7 M_\odot$ , while upcoming measurements of mid-IR flux ratios through JWST GO-02046 (PI Nierenberg) will reach  $10^6 M_\odot$ . Computing  $R_l$  for the mass range probed by existing data  $10^7 - 10^{10} M_\odot$ , we find that  $k$  scales between  $5 - 100 \text{ Mpc}^{-1}$  should contribute to the signal. Strong lenses perturbed by dark halos encode properties of the primordial matter power spectrum on scales two orders of magnitude smaller than those currently accessible by the CMB, and po-

tentially a factor of 5-10 smaller scales than those currently probed by the Lyman- $\alpha$  forest.

In this work, we push constraints on  $P(k)$  to scales  $k > 10 \text{ Mpc}^{-1}$  by performing a simultaneous inference of the concentration and abundance of low-mass dark matter halos. We then recast this measurement in terms of the primordial matter power spectrum, using theoretical models in the literature to connect the power spectrum to the halo mass function and concentration-mass relation. This work builds upon earlier work in which we have analyzed the halo mass function (Gilman et al. 2020a, e.g.) and the concentration-mass relation (e.g. Gilman et al. 2020b) independently of one another. As we will demonstrate, the joint inference of both quantities simultaneously adds crucial information that makes a strong lensing inference of  $P(k)$  possible.

This paper is organized as follows. Section 2 reviews the inference methodology and dataset used in this analysis. Section 3 discusses how the primordial matter power spectrum affects the populations of dark matter halos that strong lensing can detect, and presents the analytic model for the primordial matter power spectrum used in our analysis. Section 4 describes the models implemented in the strong lensing analysis that parameterize the halo mass function, the concentration-mass relation, the main deflector mass profile, and the lensed background source. Section 5 presents our inference of small-scale dark matter structure, and describes how we interpret this measurement in terms of the power spectrum. We summarize our findings and give concluding remarks in Section 6.

Throughout this work, we assume cosmological parameters given by WMAP9 Hinshaw et al. (2013). We perform strong lensing computations using the open source software package `lenstronomy`<sup>1</sup> (Birrer & Amara 2018; Birrer et al. 2021), and generate populations of dark matter halos for the lensing simulations using `pyHalo`<sup>2</sup> (Gilman et al. 2021). `pyHalo` makes use of `astropy` (Astropy Collaboration et al. 2018), and the open source software `colossus`<sup>3</sup> (Diemer 2018) for computations involving the halo mass function and the concentration-mass relation. We also used `galacticus` (Benson 2012) for computations of the halo mass function and concentration-mass relation with a varying primordial matter power spectrum.

## 2 INFERENCE METHODOLOGY AND DATASET

We begin by reviewing the Bayesian inference framework that we use to constrain a set of hyper-parameters describing the properties of dark matter in a sample of quads. This inference pipeline was developed and tested with simulated datasets by Gilman et al. (2018) and Gilman et al. (2019). It was then applied to real datasets to constrain models of warm dark matter (Gilman et al. 2020a), the concentration-mass relation of CDM halos (Gilman et al. 2020b), and extended to accommodate models of self-interacting dark matter (Gilman et al. 2021). In Section 2.1, we discuss the inference method, and in Section 2.2 we discuss the sample of

<sup>1</sup> <https://github.com/sibirrer/lenstronomy>

<sup>2</sup> <https://github.com/dangilman/pyHalo>

<sup>3</sup> <https://bdiemer.bitbucket.io/colossus/cosmology.html>

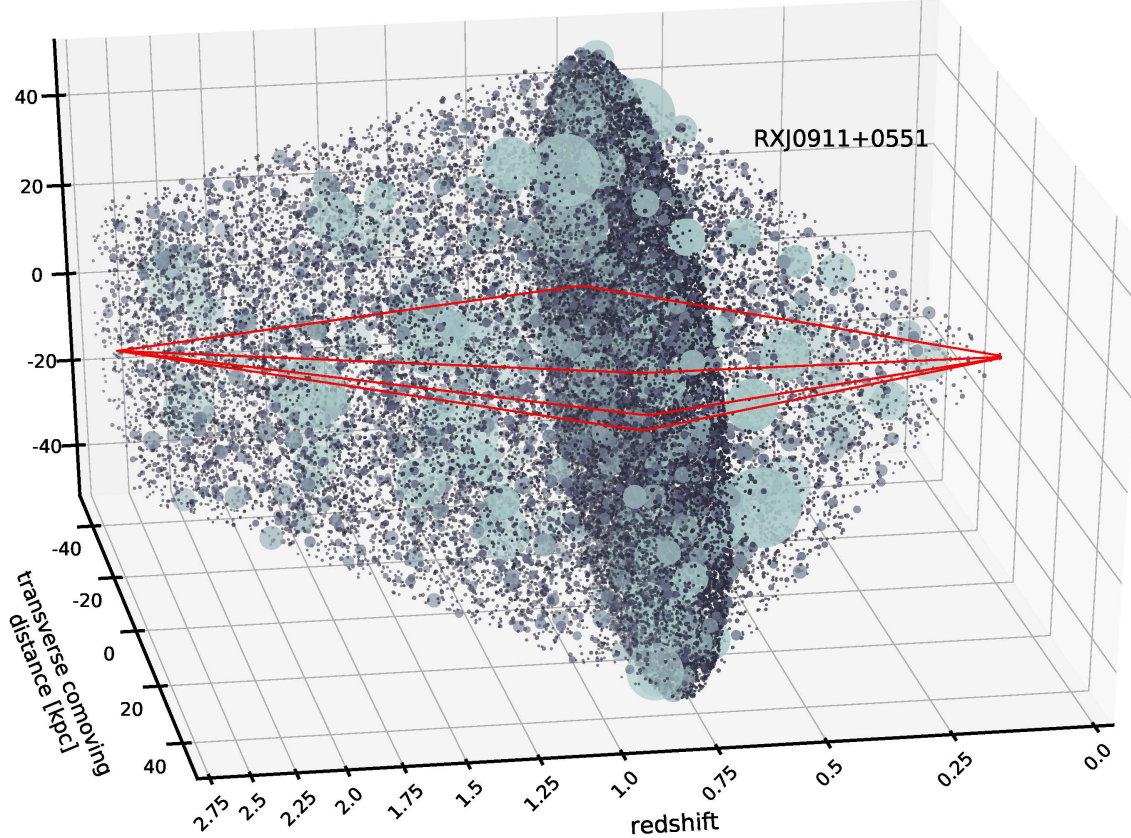


**Figure 1.** A schematic representation of the ray-tracing simulations we perform to infer the properties of dark matter structure in each lens system. The red lines show the path traversed by the light rays in the lens system RX J0911+0551. The source lies to the left, at the point of intersection of the rays. The x-axis represents the line of sight distance in redshift units between the observer and a quasar source at  $z = 2.76$ . The y and z-axes show a physical distance scale expressed as the transverse comoving separation. Black dots distributed along the line of sight represent one possible configuration of halos in the field, while subhalos of the main deflector's host dark matter halo appear packed together at the lens redshift  $z = 0.66$ . The size and color of each dot varies proportionally with the mass of the halo and its concentration, respectively.

lenses used in our analysis, most of which we have analyzed in previous work. The material unique to this paper begins in Section 3.

### 2.1 Bayesian inference in substructure lensing

Quad lens systems comprise a quasar situated behind a massive<sup>4</sup> galaxy and its host dark matter halo, which together we refer to as the main deflector. With precise alignment between the observer, source, and the main deflector, four paths through space connect the observer with the source, with the result that an observer sees four highly-magnified images of the quasar. Observables include the four image positions, and the flux of each image. As the source brightness is unknown, the relevant quantity associated with the image brightness is a magnification ratio, or a flux ratio, taken with respect to any of the four images.

The image positions and flux ratios for a sample of

lenses form a data vector  $\mathbf{D} = (\mathbf{d}_1, \mathbf{d}_2, \mathbf{d}_3, \dots)$ , with the dataset for the  $i$ th lens labeled  $\mathbf{d}_i$ . Our goal is to obtain samples from the posterior probability distribution

$$p(\mathbf{q}_s | \mathbf{D}) \propto \pi(\mathbf{q}_s) \prod_{n=1}^N \mathcal{L}(\mathbf{d}_n | \mathbf{q}_s). \quad (1)$$

The quantity  $\mathbf{q}_s$  specifies a set of hyper-parameters that describe the dark matter structure in the lens model. For the purpose of this analysis,  $\mathbf{q}_s$  specifies the slope and amplitude of the halo mass function and concentration-mass relation.

The inference method accommodates any set of parameters  $\mathbf{q}_s$ , provided we can generate individual realizations<sup>5</sup> of dark matter halos, labeled  $\mathbf{m}_{\text{sub}}$ , from the model. The individual realizations connect the hyper-parameters to observables, so we can compute the likelihood by marginalizing over all possible configurations of  $\mathbf{m}_{\text{sub}}$ , and other nuisance

<sup>4</sup> Typically an early-type galaxy residing in a  $\sim 10^{13} M_\odot$  host dark matter halo.

<sup>5</sup> By a ‘realization’ of halos, we refer to a set of coordinates, masses, and structural parameters such as the concentration, scale and truncation radii.

parameters  $\xi$

$$\mathcal{L}(\mathbf{d}_n|\mathbf{q}_s) = \int p(\mathbf{d}_n|\mathbf{m}_{\text{sub}}, \xi) p(\mathbf{m}_{\text{sub}}, \xi|\mathbf{q}_s) d\mathbf{m}_{\text{sub}} d\xi. \quad (2)$$

Directly evaluating the integral in Equation 4, however, presents an insurmountable challenge. Most configurations of  $\mathbf{m}_{\text{sub}}$  and  $\xi$  produce a lens that looks nothing like the data, and hence only a small volume of parameter space contributes to the integral.

To make the evaluation of Equation 4 tractable, we focus computational resources on specific combinations of  $\xi$  and  $\mathbf{m}_{\text{sub}}$  that, by construction, match the image positions of the observed dataset  $\mathbf{d}_n$ . We target the small volume of parameter space that contributes to the likelihood integral by solving for a set of parameters (contained in  $\xi$ ) describing the main lensing galaxies' mass profile that map the four observed image positions to a common source position in the presence of the full population of dark matter subhalos and line of sight halos specified by  $\mathbf{m}_{\text{sub}}$ . This task amounts to a non-linear optimization problem using the recursive form of the multi-plane lens equation (Blandford & Narayan 1986)

$$\boldsymbol{\theta}_K = \boldsymbol{\theta} - \frac{1}{D_s} \sum_{k=1}^{K-1} D_{ks} \boldsymbol{\alpha}_k (D_k \boldsymbol{\theta}_k). \quad (3)$$

In the preceding equation,  $\boldsymbol{\theta}_k$  is the angular coordinate of a light ray on the  $k$ th lens plane,  $\boldsymbol{\theta}$  is a coordinate on the sky,  $D_k$  represents the angular diameter distance to the  $k$ th lens plane,  $D_{ks}$  represents the angular diameter distance from the  $k$ th lens plane to the source plane, and  $\boldsymbol{\alpha}_k$  is the deflection field at the  $k$ th lens plane that includes the contributions from all dark matter halos at that redshift. The dimension of the optimization problem depends on the number of free parameters describing the main deflector mass profile. We return to this topic when describing the lens model for the main deflector in Section 4.2.

With a combination of  $\xi$  and  $\mathbf{m}_{\text{sub}}$  that produces a lens system with the same image positions as in the data, we can proceed to compute the model flux ratios at the correct image positions. At this stage, however, the task at hand still seems insurmountable because marginalizing over all possible configurations of halos specified by  $\mathbf{m}_{\text{sub}}$  involves, for all intents and purposes, an infinite number of lensing computations. However, we can again reduce the computational expense by sampling from the likelihood function in Equation 2 with an Approximate Bayesian Computing approach (Rubin 1984). Given the flux ratios of the observed dataset  $\mathbf{f}_{\text{obs}}$  and a set of model-predicted flux ratios  $\mathbf{f}_{\text{model}}$ , we compute a summary statistic

$$S \equiv \sqrt{\sum_{i=1}^3 (f_{\text{obs}(i)} - f_{\text{model}(i)})^2}, \quad (4)$$

and accept proposals of  $\mathbf{q}_s$  with the condition  $S < \epsilon$ , where  $\epsilon$  represents a tolerance threshold. As  $\epsilon$  approaches zero, the ratio of the number of accepted samples between two models  $\mathbf{q}_{s1}$  and  $\mathbf{q}_{s2}$  approaches the relative likelihood of the models  $\frac{\mathcal{L}(\mathbf{d}_n|\mathbf{q}_{s1})}{\mathcal{L}(\mathbf{d}_n|\mathbf{q}_{s2})}$ , allowing us to approximate the intractable likelihood function in Equation 2, up to a constant numerical factor. We can then multiply the likelihoods obtained

from individual lenses to obtain the posterior distribution in Equation 1<sup>6</sup>.

Figure 1 shows a schematic example of one lens system RX J0911+0551, with a full population of subhalos and line of sight halos included in the lens model. The red lines depict the path of lensed light rays through lines of sight populated by halos; roughly 10,000 halos appear in the figure. For the analysis presented in this paper, we repeat this procedure  $\mathcal{O}(10^6)$  times per lens, and retain the top 3,500 samples to compute the likelihood.

## 2.2 Lens sample

Our lens sample consists of eleven quadruply-imaged quasars. Each system meets two criteria designed to mitigate sources of systematic error in the flux ratio measurements and the lens modeling.

First, each lens in the sample has flux ratios computed from either [OIII] doublet emission at 4960Å and 5007Å that emanates from the nuclear narrow line region (NLR), or radio emission from a more compact area surrounding the background quasar. For a typical source redshift, both the NLR and radio emission regions subtend angular scales greater than 1 milli-arcsecond on the sky, removing the contaminating effects of microlensing by stars in the main deflector but preserving sensitivity to milli-arcsecond scale deflections produced by dark matter halos. Exploiting differential magnification by finite-size sources eliminates microlensing as a source of systematic error, but in turn it requires explicit modeling, which we account for in our analysis.

The second criterion we impose demands that the main deflector show no evidence for stellar disks, as these structures require explicit treatment in the lens modeling (Gilman et al. 2017; Hsueh et al. 2016, 2017). Stellar disks appear prominently with current imaging data, allowing for the rapid identification and removal of problematic systems from the lens sample.

The lenses in our sample with narrow-line flux measurements, and the corresponding reference for the astrometry and image fluxes are RXJ 1131+0231 (Sugai et al. 2007), B1422+231 (Nierenberg et al. 2014), HE0435-1223 (Nierenberg et al. 2017), WGD J0405-3308, RX J0911+0551, PS J1606-2333, WFI 2026-4536, WFI 2033-4723, WGD 2038-4008 (Nierenberg et al. 2020). The two systems in our sample with radio flux measurements are PG 1115+080 (Chiba et al. 2005), and MG0414+0534 (Stacey et al. 2020). The only quad in our system that we have not included in a previous work is RXJ 1131+0231. For this work, we expanded our lensing simulation pipeline to model the asymmetric narrow-line emission around the background quasar discussed by Sugai et al. (2007).

<sup>6</sup> Before combining the likelihoods for individual lenses, we apply Gaussian kernel density estimator (KDE) with a first-order correction to the likelihood at the edge of the prior to remove edge effects. Applying the KDE results in a smooth interpolation of the likelihood, reducing shot noise when multiplying several discretely-sampled, but high-dimensional, probability distributions.

### 3 CONNECTING THE PRIMORDIAL MATTER POWER SPECTRUM TO DARK MATTER STRUCTURE

A challenging aspect of inferring  $P(k)$  from astronomical data – whether from the CMB, the Lyman- $\alpha$  forest, or strong lensing – stems from the simple fact that the power spectrum itself is not directly observable. In the case of strong lensing, the amount of perturbation to image magnifications in quads depend on the overall amount of structure, as determined by the mass function  $n(m, z)$  (e.g. Gilman et al. 2020a), and the central density, or lensing efficiency, of halos determined by the concentration mass relation  $c(m, z)$  (e.g. Gilman et al. 2020b; Amorisco et al. 2021; Minor et al. 2021), with the result that a strong lensing measurement connects to  $P(k)$  through the  $n(m, z)$  and  $c(m, z)$  relations.

To cast a strong lensing measurement in terms of  $P(k)$ , we require a specific model for  $P(k)$ , and a way to compute  $n(m, z)$  and  $c(m, z)$  from it in the mass range relevant for substructure lensing  $10^7 - 10^{10} M_\odot$ . In Section 3.1, we describe the theoretical models that connect  $n(m, z)$  and  $c(m, z)$  to  $P(k)$ . Next, in Section 3.2, we describe the parameterization for  $P(k)$  used in this analysis, and in Section 3.3 we illustrate how changes to the power spectrum on small scales manifest in the abundance and concentrations of halos.

#### 3.1 Theoretical models for halo abundance and internal structure

Before discussing in detail the technical aspects of how the primordial matter power spectrum determines the properties of dark matter halos, we can make qualitative predictions for the effects on dark matter structure that would result from an increase in power at a particular (but arbitrary) scale  $\tilde{k}$ , which corresponds to a halo mass scale  $\tilde{m} \propto \tilde{k}^{-3}$ . First, adding power at  $\tilde{k}$  increases the fraction of volume elements in the Universe that collapse into halos of mass  $\tilde{m}$ . The mass function  $n(m, z)$  therefore connects to  $P(k)$  by enumerating how many peaks in the density field collapse into a halo of mass  $m$  (Press & Schechter 1974). Second, increasing the amplitude of fluctuations at the scale  $\tilde{k}$  causes fluctuations on this scale to collapse earlier, accelerating the formation of halos of mass  $\tilde{m}$  relative to a scenario with no enhancement of power at  $\tilde{k}$ . The central density of a halo reflects the background density of the Universe when the halo formed, and because the expansion of space relentlessly dilutes the background density, halos that collapsed earlier will have higher central densities than halos that collapsed later. Thus, the concentration-mass relation  $c(m, z)$ , which predicts the median central density of a halo as a function of mass and redshift, connects to  $P(k)$  through the timing of structure formation (Navarro et al. 1997; Bullock et al. 2001; Eke et al. 2001; Wechsler et al. 2002).

##### 3.1.1 The halo mass function

The halo mass function has a concrete, analytic connection to  $P(k)$  through the variance of the density field  $\sigma(R_l, z)$

$$\sigma^2(R_l, z) = \frac{D(z)^2}{2\pi^2} \int_{-\infty}^{\infty} k^2 P_{\text{lin}}(k) \tilde{W}^2(kR_l) dk, \quad (5)$$

where  $\tilde{W}(kR_l)$  is the Fourier transform of the spherical top-hat window function,  $D(z)$  is the linear growth function for the perturbations, and  $R_l = \left( \frac{3M}{4\pi\Omega_m \rho_{\text{crit}}} \right)^{\frac{1}{3}}$  is the Lagrangian radius of the halo computed with the fractional contribution of matter,  $\Omega_m$ , to the critical density of the Universe  $\rho_{\text{crit}}$ . We have also introduced the linear theory matter power spectrum,  $P_{\text{lin}}(k) \equiv P(k) T(k)^2$ , as the primordial matter power spectrum times the square of the transfer function  $T(k)$  presented by Eisenstein & Hu (1998). The number of halos per logarithmic mass interval  $\log m$  per unit volume depends on  $\sigma$  through

$$\frac{d^2 N}{d \log m \, dV} \equiv n(m, z) = f(\sigma, z) \frac{\rho_0}{m} \frac{d \log \sigma^{-1}}{d \log m} \quad (6)$$

where  $f(\sigma, z)$  represents the fraction of mass contained in halos for a given variance.

Over the last two decades, several mass function models have appeared in the literature with different parameterizations for  $f(\sigma, z)$ . We use as a baseline the model presented by Sheth et al. (2001), hereafter referred to as Sheth-Tormen. The Sheth-Tormen model extended Press-Schechter formalism (Press & Schechter 1974) to models of ellipsoidal collapse, with the inclusion of two free parameters,  $a$  and  $p$ , calibrated against simulations. The Sheth-Tormen mass function has

$$\nu f(\nu) = A \left( 1 + \frac{1}{\nu^p} \right) \left( \frac{\nu'}{2} \right)^{\frac{1}{2}} \frac{e^{-\frac{\nu'}{2}}}{\sqrt{\pi}}, \quad (7)$$

where  $\nu' \equiv a\nu(m, z)^2$ , where  $\nu(m, z) = \delta_c/\sigma$  is the peak height in terms of the variance  $\sigma$ , and  $\delta_c = 1.686$  is the overdensity threshold for spherical collapse in an Einstein de-Sitter universe. Bohr et al. (2021) recently compared the predictions of Sheth-Tormen model on halo mass scales  $\sim 10^7 M_\odot$  and found excellent agreement with their simulations, although the simulations only evolved structure until  $z = 5$ .

Most other mass function models presented to date either re-calibrate the Sheth-Tormen model to different cosmologies (e.g. Despali et al. 2016), or empirically adjust it to match the high-mass end of the mass function to higher precision (e.g. Tinker et al. 2008). Each model makes modestly different predictions for the slope and amplitude of the mass function on the mass scales of interest, which could in principle affect our results, so we perform the analysis described in the remainder of this paper using two other forms for  $f(\sigma, z)$ . In the end, however, we find that the statistical measurement uncertainties of our main result are larger than the effect of assuming a different model for the halo mass function. For the remainder of the paper, we therefore assume the model  $f(\sigma, z)$  presented Sheth-Tormen. Appendix B recreates our main results using the other two mass function models we considered.

##### 3.1.2 The concentration-mass relation

To connect halo concentrations to the power spectrum, we use the concentration-mass relation model presented by Diemer & Joyce (2019), which provides a particularly accurate fit for the concentrations of low-mass halos relevant for a lensing analysis with quads. The model predicts halo

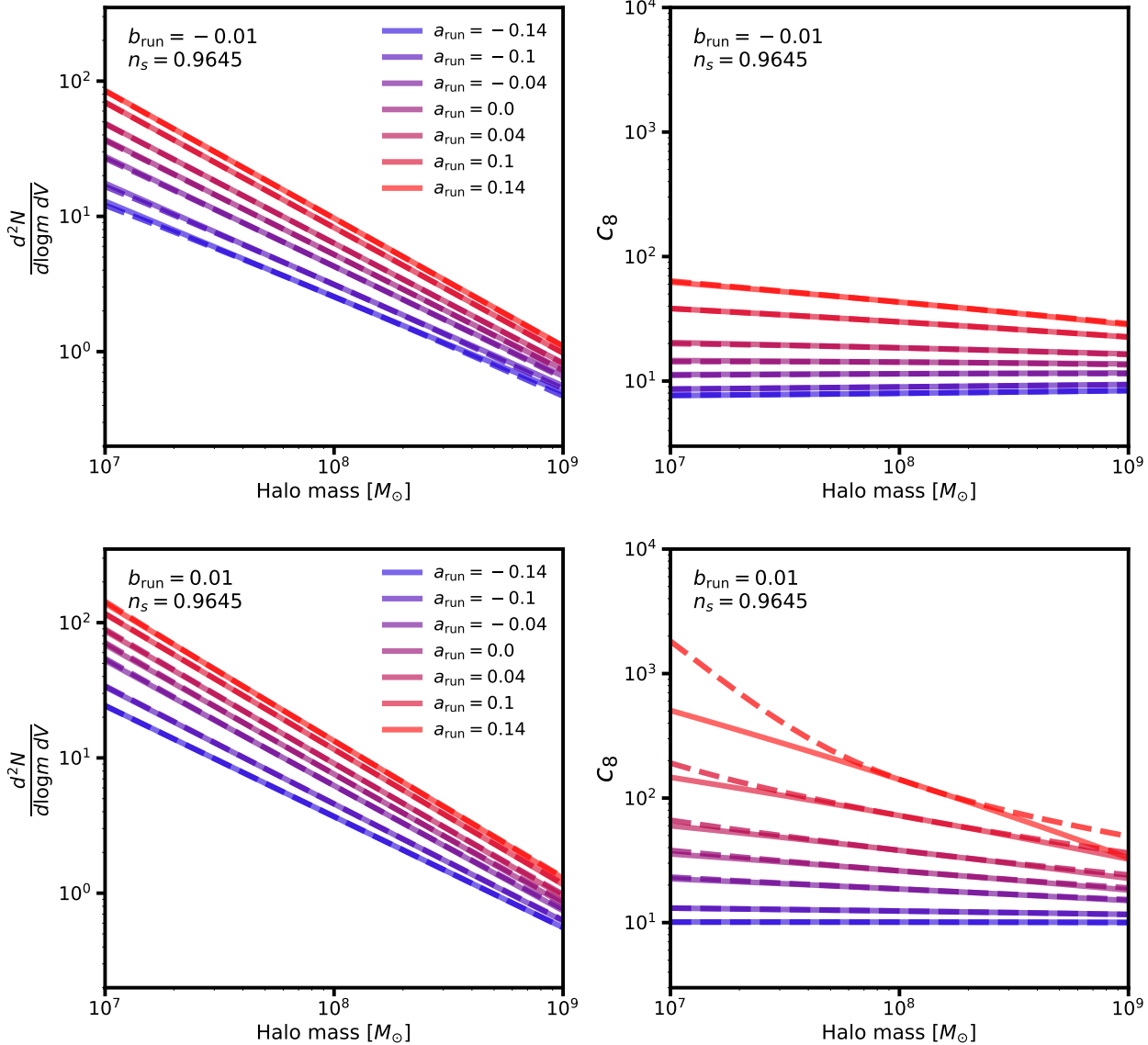


**Figure 2.** Theoretical predictions (solid lines) and model fits (dashed lines, see Section 5.2) to the halo mass function (left) and concentration-mass relation (right) as a function of  $a_{\text{run}}$  and  $b_{\text{run}}$ , the parameters that determine the scale dependence of the spectral index of the primordial matter power spectrum on scales  $k > 1 \text{ Mpc}^{-1}$ . Increasing small-scale power through positive values of  $a_{\text{run}}$  and  $b_{\text{run}}$  makes halos more concentrated and more abundant, while decreasing small-scale power makes them less abundant and less concentrated. The curves in the figures use a fixed value of the spectral index  $n_s$ , but the effects of varying  $n_s$  are qualitatively similar to the effects of adding power through  $a_{\text{run}}$  and  $b_{\text{run}}$ .

concentration  $c$  by solving

$$c = F^{-1} \left[ \frac{\Omega_m(z)}{\Omega_m(z_{\text{pe}})} \frac{1+z_{\text{pe}}}{1+z} F(c_{\text{pe}}) \right] \quad (8)$$

where  $F(x) = \log(1+x) - \frac{x}{1+x}$  for Navarro-Frenk-White (NFW) (Navarro et al. 1997) profiles,  $F^{-1}(F(x)) = x$ , and  $\Omega_m$  represents the fraction of the critical density of the Universe composed of matter. The quantities  $c_{\text{pe}}$  and  $z_{\text{pe}}$  refer to the concentration and redshift at the time the halo concentration began changing through ‘pseudo-evolution’, which refers to a change in halo concentration due to the evolution of the background density of the Universe, even though the physical structure of the halo remains fixed (Diemer et al. 2013).

Diemer and Joyce connect the power spectrum to halo concentrations by postulating that  $c(m, z)$  depends on both the epoch of halo formation, and on the effective slope of the power spectrum evaluated near the Lagrangian radius of a halo  $\partial \log P / \partial \log k|_{R=\kappa R_l}$ . They assume a linear relationship between  $c_{\text{pe}} = a + b(\tilde{n}(k) + 3)$ , and an effective logarithmic slope  $\tilde{n}(k) \equiv -2 \frac{d \log \sigma}{d \log R}|_{R=\kappa R_l} - 3$ . The paper by Diemer and Joyce gives additional details about the calibration of this model using simulations with a variety of power spectra, which the authors use to determine the best-fit values of  $a$ ,  $b$ , and  $\kappa$ .

### 3.2 A model for the primordial matter spectrum $P(k)$

In order to connect the primordial matter power spectrum  $P(k)$  to observables, we must be able to integrate it to compute the variance  $\sigma(R_l, z)$ , and differentiate it to compute the logarithmic slope of the power spectrum  $\frac{\partial \log P}{\partial \log k} \big|_{R=\kappa R_l}$ . These practical considerations, together with the limiting constraining power of existing data, disfavor a completely free-form model for  $P(k)$  where we vary the amplitude in different  $k$  bins. Instead, given the precise measurements of the power spectrum on scales  $k < 1 \text{ Mpc}^{-1}$  by a number of different methods, we anchor  $P(k)$  on large scales, and allow the small-scale amplitude to vary assuming a functional form given by

$$P(k) = \begin{cases} P_{\Lambda\text{CDM}}(k) & k \leq k_0 \\ P_{\Lambda\text{CDM}}(k_0) \left(\frac{k}{k_0}\right)^{n(k)} & k > k_0 \end{cases} \quad (9)$$

where we define  $P_{\Lambda\text{CDM}} \equiv P_0 \left(\frac{k}{k^*}\right)^{-0.9645}$  with the normalization  $P_0$  and spectral index  $n_s$  fixed to the latest analyses of CMB data (Planck Collaboration et al. 2020c) with  $k^* = 0.05 \text{ Mpc}^{-1}$ . The function  $n(k)$  specifies a scale-dependent spectral index that we expand to second order in  $\log k$ <sup>7</sup>

$$n(k) = n_s + a_{\text{run}} \log\left(\frac{k}{k_0}\right) + b_{\text{run}} \log\left(\frac{k}{k_0}\right)^2 \quad (10)$$

around a pivot scale  $k_0 = 1 \text{ Mpc}^{-1}$ . This parameterization is motivated in part by the predictions of slow roll inflation, which predicts a hierarchy of coefficients for the scale-dependent terms  $\frac{b_{\text{run}}}{a_{\text{run}}} \sim |n_s - 1|$ . We do not vary the normalization of the power spectrum because the uncertainty in the overall normalization, as inferred from the CMB, is completely negligible in terms of its effect on the mass function and concentration-mass relation relative to the effect of varying  $n_s$ ,  $a_{\text{run}}$ , and  $b_{\text{run}}$ .

The optimal choice for the pivot scale depends on the sensitivity of the dataset used to constrain the power spectrum. For the dataset relevant for this analysis, we estimate sensitivity to halos with masses down to  $10^7 M_\odot$ , corresponding to  $k \sim 100 \text{ Mpc}^{-1}$ . However, because halo abundance and structure depends on integrals and derivatives of  $P(k)$ , a range of  $k$  scales affect the properties of halos of any given mass. Further, halos of different mass contribute in varying degree to the signal we extract from the data. Given these complications, we perform our analysis using a number of different pivot scales in the range  $0.1 - 5 \text{ Mpc}^{-1}$ . Discussion of how the position of the pivot scale affects our main result can be found in Appendix B.

### 3.3 Predicting halo abundance and concentration from $P(k)$

Assuming the functional form for the power spectrum in Equation 9 in terms of  $n_s$ ,  $a_{\text{run}}$ , and  $b_{\text{run}}$ , the variance  $\sigma$  and the effective logarithmic slope  $\tilde{n}(k)$  are both implicitly functions of these parameters, i.e.  $\sigma \equiv \sigma(R_l, z, n_s, a_{\text{run}}, b_{\text{run}})$

<sup>7</sup>  $\log$  refers to a natural logarithm, unless it is explicitly written with base 10.

and  $\tilde{n}(k) \equiv \tilde{n}(k, n_s, a_{\text{run}}, b_{\text{run}})$ . Thus, we can compute the mass function and concentration-mass relation for any  $n_s, a_{\text{run}}, b_{\text{run}}$ . We perform these computations using the semi-analytic modeling software **galacticus** (Benson 2012).

Figure 2 shows, in solid lines, the theoretically-predicted mass functions and concentration-mass relations for different combinations of  $a_{\text{run}}$  and  $b_{\text{run}}$  for the Sheth-Tormen mass function, using the model for  $P(k)$  in Equation 9. The dashed lines show fits to these relations in terms of parameters we will constrain with a lensing analysis (see Section 5). The three mass function models we consider (see Appendix B for results using models other than Sheth-Tormen) exhibit similar trends with small-scale changes to  $P(k)$ .

As discussed at the beginning of this section, and as Figure 2 clearly demonstrates, increasing small-scale power leads to covariant changes in the amplitude of the halo mass function and concentration-mass relation. Since strong lensing data is sensitive to both halo abundance and concentration, we expect significant constraining power over the power spectrum parameters from a sample of quadruply-imaged quasars. To extract this signal, we perform a strong-lensing inference of the halo mass function and concentration-mass relation. We discuss the models implemented in the lensing analysis in the following section.

## 4 MODELS IMPLEMENTED IN THE STRONG LENSING ANALYSIS

In this section, we describe the structure formation and lens models used to infer the properties of dark matter halos with masses below  $10^{10} M_\odot$ . First, Section 4.1 describes the parameterization of the halo and subhalo mass functions, and the concentration-mass relation. Section 4.2 describes our model for the mass profile of the main lensing galaxy (the ‘main deflector’), and Section 4.3 discusses how we model the finite-size of lensed background source.

### 4.1 Parameterization of the halo mass function and concentration-mass relation

Two distinct populations of dark matter halos perturb strongly lensed images: field halos along the line of sight, and subhalos around the host dark matter halo. In this section, we discuss the analytic expressions for the mass function and concentration-mass relation for each of these populations of halos, parameterized by hyper-parameters whose joint likelihood we will compute in the lensing analysis. Our goal will eventually be to connect the models described in this section to the theoretical predictions for the mass function and concentration-mass relation described in the previous section to cast the lensing inference in terms of  $P(k)$ . Notation used throughout this and the remaining sections is summarized in Table 1, and we summarize all model parameters discussed in this section in Table 2.

#### 4.1.1 Model for the halo and subhalo mass functions

We generate realizations of line-of-sight halos by sampling halo masses in the range  $10^6 - 10^{10} M_\odot$  from a mass function

parameterized as

$$\frac{d^2N}{d\log m dV} = \delta_{\text{LOS}} \left( \frac{m}{m_0} \right)^{\Delta\alpha} [1 + \xi_{\text{halo}}(M_{\text{host}}, z)] \frac{d^2N_0}{d\log m dV} \quad (11)$$

where  $\frac{d^2N_0}{d\log m dV}$  represents the Sheth-Tormen mass function model evaluated with  $n_s = 0.9645$ ,  $a_{\text{run}} = 0$ , and  $b_{\text{run}} = 0$ . Halos less massive than  $10^6 M_\odot$  have lensing effects too weak to affect the flux ratios in our dataset given the source sizes we consider, while halos more massive than  $10^{10} M_\odot$  would likely host a visible galaxy, in which case we would explicitly include them in the lens model. To account for how the mass function responds to changes in the power spectrum, we include a free normalization factor  $\delta_{\text{LOS}}$  and logarithmic slope  $\Delta\alpha$ . We also add a contribution from the two-halo term  $\xi_{\text{2halo}}$ <sup>8</sup>, which accounts for the presence of correlated structure around the host dark matter halo with mass  $M_{\text{host}}$  (Lazar et al. 2021).

To model subhalos of the host dark matter halo, we sample masses from a subhalo mass function defined in projection, which we parameterize as

$$\frac{d^2N}{dm dA} = \Sigma_{\text{sub}} \left( \frac{m}{m_0} \right)^{\alpha+q\Delta\alpha} \mathcal{F}(M_{\text{halo}}, z), \quad (12)$$

where  $\mathcal{F}(M_{\text{halo}}, z)$  accounts for the evolution of the projected mass in substructure with the host halo mass and redshift (Gilman et al. 2020a). Factoring the evolution with host halo mass and redshift out of  $\Sigma_{\text{sub}}$  allows us to combine inferences of the parameter from different lenses, in host halos with different masses at various redshifts. The normalization  $\Sigma_{\text{sub}}$  also absorbs the effects of tidal stripping. We expect a similar amount of tidal stripping among the lenses in our sample because the host halos have similar masses of  $\sim 10^{13} M_\odot$  with elliptical galaxies at their centers.

The subhalo mass function has a logarithmic slope  $\alpha+q\Delta\alpha$ , where  $\alpha$  is the CDM prediction for the logarithmic slope  $\alpha \sim -1.9$  (Springel et al. 2008), and  $\Delta\alpha$  is the same variation in logarithmic slope we apply to the field halo mass function. As the host dark matter halo accretes its subhalo population from the field, we expect the subhalo mass function to have a similar logarithmic slope to the field halo mass function, but we allow for some flexibility in this connection by introducing the parameter  $q$ . For our analysis, we assume a uniform prior on  $q \sim \mathcal{U}(0.7, 1.0)$ , such that the logarithmic slopes of the subhalo and field halo mass functions vary nearly in tandem.

#### 4.1.2 Model for the concentration-mass relation

We model the mass-concentration relation as a power law in peak height, a parameterization that accurately reproduces concentration-mass relations predicted by simulations of structure formation (Prada et al. 2012; Gilman et al. 2020b). We assume a functional form given by

$$c(m, z) = c_8 (1+z)^\zeta \left( \frac{\nu_0(m, z)}{\nu_0(10^8, 0)} \right)^{-\beta}. \quad (13)$$

where we have defined  $\nu_0 \equiv \delta_c/\sigma(m, z, 0.9645, 0, 0)$  as the peak height evaluated for a power spectrum with spectral

<sup>8</sup> for details, see Gilman et al. (2019)

index  $n_s = 0.9645$ ,  $a_{\text{run}} = 0$ , and  $b_{\text{run}} = 0$ . We account for changes to halo concentrations from the power spectrum through a flexible normalization  $c_8$ , and logarithmic slope  $\beta$ . We introduce an additional term  $(1+z)^\zeta$  to slightly modify the redshift evolution in order to match the redshift evolution predicted by concentration-mass relations studied in the literature. The results we present are marginalized over a uniform prior on  $\zeta$  between -0.3 and -0.2.

We evaluate the concentration-mass relation at the halo redshift for field halos. For subhalos, we evaluate their concentrations at the infall redshift, which we predict using *galacticus* (Benson 2012). The distinction between subhalo and field halo concentrations arises because pseudo-evolution, or a changing concentration parameter due to the changing background density of the Universe, determines the redshift evolution of  $c(m, z)$  for low-mass halos in the field (Diemer & Joyce 2019). As soon as a field halo crosses the virial radius of its future host and becomes a subhalo, it follows an evolutionary track determined by the tidal field of the host halo, and the elliptical galaxy at its center (Green & van den Bosch 2019); the concept of ‘pseudo-growth’ no longer applies. Finally, we note that evaluating subhalo concentrations at infall implies the mass definition of the  $m_{200}$  evaluated at infall, rather than the time of lensing. We account for tidal evolution of subhalos between the time of infall and the time of lensing by truncating their density profiles.

#### 4.1.3 Model for halo density profiles

We model the density profiles of both field halos and subhalos as truncated NFW profiles (Baltz et al. 2009)

$$\frac{\rho(c, x, \tau)}{\rho_{\text{crit}}(z')} = \frac{c^3}{\log(1+c) - \frac{c}{1+c}} \left( \frac{\tau^2}{x(1+x)^2(x^2+\tau^2)} \right) \quad (14)$$

with  $x = r/r_s$  and  $\tau = r_t/r_s$ , with truncation radius  $r_t$ . We have explicitly defined the profile in terms of the concentration  $c$ , and  $\rho_{\text{crit}}(z')$ , the critical density of the Universe at redshift  $z'$ , which represents either the halo redshift (for field halos), or the infall redshift (for subhalos). We tidally truncate subhalos according to their three dimensional position inside the host halo (see Gilman et al. 2020a), and truncate field halos at  $r_{50}$ , comparable to the halo splashback radius (More et al. 2015).

## 4.2 Main deflector lens model

As we omit lens systems with stellar disks, the remaining systems have structural properties typical of the early-type galaxies that dominate the strong lensing cross section, with roughly elliptical isodensity contours and an approximately isothermal logarithmic profile slope  $\gamma$  (Auger et al. 2010). These observations motivate the use of a power-law ellipsoid for the main mass profile with a logarithmic slope  $\gamma$  sampled from a uniform prior ranging between -1.9 and -2.2. If the lens system has a luminous satellite detected in the imaging data, we model it as a singular isothermal sphere with astrometric uncertainties of 50 m.a.s., and set the Einstein radius to the value determined by the discovery papers. Following common practice, we account for structure further away from the main deflector by embedding the power-law

ellipsoid model in an external tidal field with shear strength  $\gamma_{\text{ext}}$ . We assume a uniform prior on  $\gamma_{\text{ext}}$  that we determine on a lens-by-lens basis<sup>9</sup>.

To account for deviations from purely elliptical isodensity contours in the main lens profile, we add an octopole mass moment with amplitude  $a_4$  aligned with the position angle  $\phi_0$  of the main deflector's mass profile. The octopole mass moment is given by

$$\kappa_{\text{oct}}(r) = \frac{a_4}{r} \cos(4(\phi - \phi_0)). \quad (15)$$

For positive (negative) values of  $a_4$ , the inclusion of  $\kappa_{\text{oct}}$  produces disk-like (boxy) isodensity contours. The inclusion of this term increases the flexibility of the main deflector lens model, mitigating sources of systematic error that may arise from an overly-simplistic model for the main deflector Gilman et al. (2017); Hsueh et al. (2018). For each system, we marginalize over a uniform prior on  $a_4$  between  $-0.01$  and  $0.01$ . This range of  $a_4$  reproduces the range of boxiness and diskyness observed in the surface brightness contours of elliptical galaxies Bender et al. (1989). Because the boxiness or diskyness of the light profile should exceed the boxiness or diskyness of the projected mass profile after accounting for the contribution of the host dark matter halo, this prior introduces the maximum reasonable amount of uncertainty in the main deflector's boxiness or diskyness.

When solving for a set of macromodel parameters that map the observed image coordinates to the source position with Equation 3, we allow the Einstein radius, mass centroid, axis ratio, axis ratio position angle, the position angle of the external shear, and the source position, to vary freely. We sample the logarithmic profile slope, the strength of the external shear, and the amplitude of the octopole mass moment, from uniform priors (see Table 2), and keep their values fixed during the lensing computations performed for each realization of dark matter halos.

### 4.3 Background source model

The effect of a halo with a fixed mass profile on the magnification of a lensed image depends on the size of the background source (Dobler & Keeton 2006; Inoue & Chiba 2005). We account for finite-source effects in the data by computing flux ratios with a finite-source size in the forward model. For systems with flux ratio measurements from the nuclear narrow-line region, we marginalize over a uniform prior on the source size between  $25 - 60$  pc (Müller-Sánchez et al. 2011), and for the radio emission we marginalize over a uniform prior between  $1 - 20$  pc (Stacey et al. 2020). We model the source as a Gaussian, and when quoting its size refer to the full width at half maximum. We compute the image magnifications by ray-tracing through the lens model, and integrate the total flux from the source that appears in the image plane.

The only exception to the source modeling described

<sup>9</sup> We eventually constrain  $\gamma_{\text{ext}}$  itself when we select models the fit the data using the summary statistic computed from each flux ratio. To choose an appropriate prior, we initially sample a wide range of  $\gamma_{\text{ext}}$  to determine what values can fit the observed flux ratios. Based on this initial estimate, we then focus the sampling on a more restricted range of  $\gamma_{\text{ext}}$  for each system.

in the previous paragraph applies to the lens system RXJ1131+1231, which has NLR flux ratio measurements presented by Sugai et al. (2007). Sugai et al. (2007) show that the NLR surrounding the quasar in this lens system appears to have an asymmetric structure that extends to the north. We model this additional source component by adding a second Gaussian light profile to the north of the main NLR, with a spatial offset between it and the main NLR that we allow to vary freely between  $0-80$  parsecs. In addition, we rescale both the size and surface brightness of the second source component relative to the size and surface brightness of the main NLR by random factors sampled between  $0.3 - 1$ . We marginalize over both the size of the main NLR, and the spatial offset, size, and brightness of the second source component in our analysis.

## 5 CONSTRAINTS ON $P(k)$

This section presents our main result: an inference of the primordial matter power spectrum on small scales obtained from a measurement of halo abundance and internal structure using eleven quadruply-imaged quasars. Table 1 summarizes the notation that appears frequently throughout this section. We divide the presentation of our main results into three subsections.

First, Section 5.1 describes how we use the models for the halo mass function and concentration-mass relation described in the previous section to compute the probability of  $\mathbf{q}_s = (\delta_{\text{LOS}}, \beta, \log_{10} c_8, \Delta\alpha, \Sigma_{\text{sub}})$  given the data, or  $p(\mathbf{q}_s | \mathbf{D})$ . We then briefly comment on the results, which have standalone value as a detailed inference of the properties of low-mass dark matter halos and subhalos. Second, Section 5.2 describes how we translate the constraints on the  $\mathbf{q}_s$  parameters sampled in the lensing analysis to constraints on the parameters  $\mathbf{q}_p \equiv (n_s, a_{\text{run}}, b_{\text{run}})$  that describe the power spectrum. We then present an inference of  $p(\mathbf{q}_p | \mathbf{D})$ , or the joint constraints on the  $\mathbf{q}_p$  parameters given the data. Finally, Section 5.3 describes how we use the probability distribution  $p(\mathbf{q}_p | \mathbf{D})$  to infer the amplitude of  $P(k)$  at different  $k$  scales, assuming the model for the power spectrum in Equation 9.

### 5.1 Joint inference of the halo mass function and concentration-mass relation

Applying the inference framework described in Section 2 to the structure formation model described in Section 4, we compute the joint probability distribution of the hyperparameters  $\mathbf{q}_s$  that describe the subhalo and halo mass functions, and the concentration mass relation. Figure 3 shows the posterior distribution  $p(\mathbf{q}_s | \mathbf{D})$ . The  $\Lambda$ CDM prediction for each parameter is marked in black. The amplitude of the subhalo mass function  $\Sigma_{\text{sub}}$  depends, among other factors, on the tidal stripping efficiency of the massive elliptical galaxies that act as strong lenses. For this reason, we do include a  $\Lambda$ CDM prediction for  $\Sigma_{\text{sub}}$  in the figure. We note that the binning and the kernel density estimator applied to the individual lens likelihoods slightly alters the probability

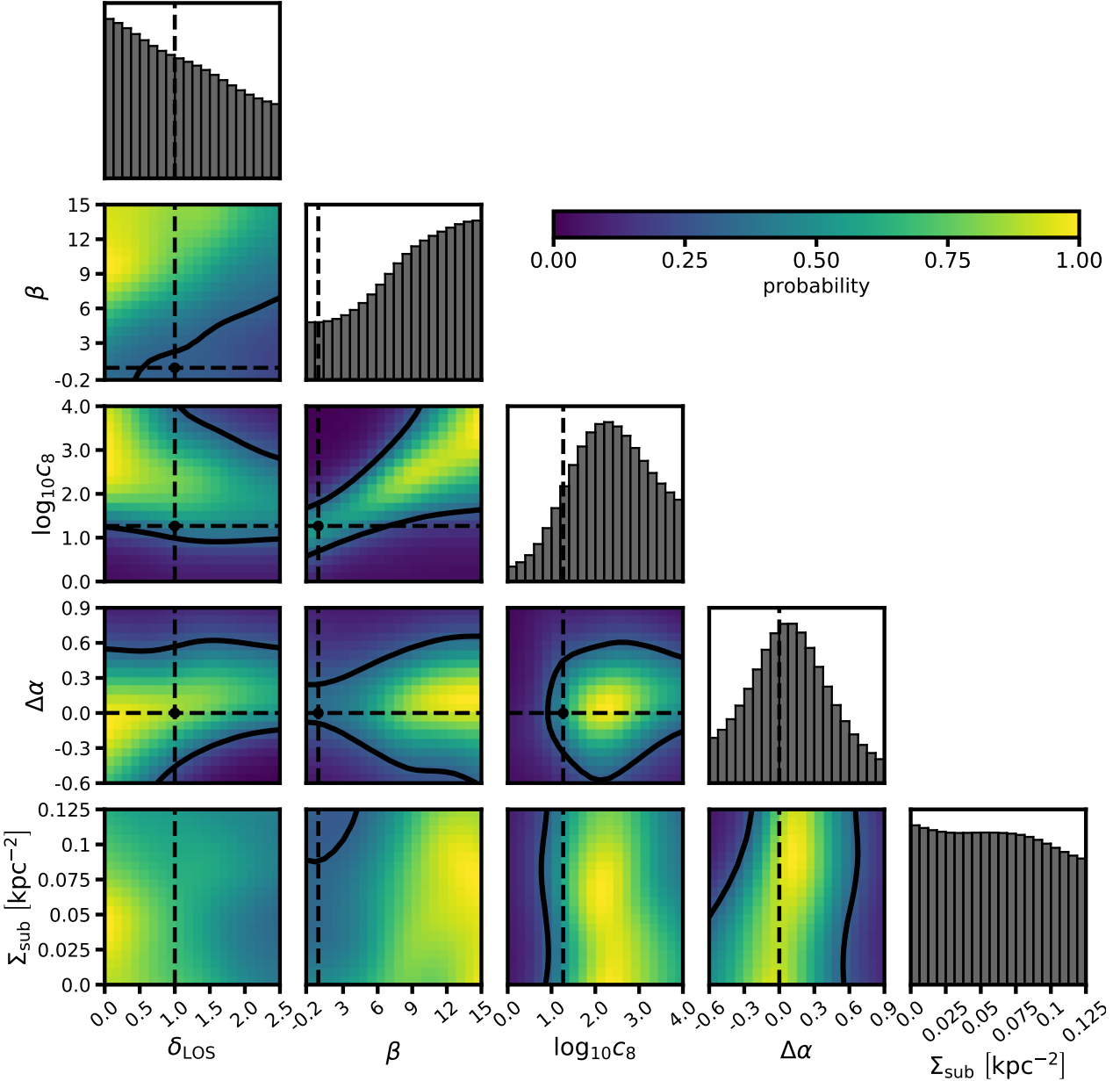


**Figure 3.** The joint probability distribution  $p(\mathbf{q}_s|\mathbf{D})$  obtained by applying the inference method described in Section 2 to a sample of eleven quads. The parameters in  $\mathbf{q}_s$ , which we summarize in Table 2, include  $\Sigma_{\text{sub}}$ , the amplitude of the subhalo mass function, and  $\delta_{\text{LOS}}$ , the amplitude of the field halo mass function relative to the prediction of the Sheth-Tormen model in  $\Lambda\text{CDM}$ . We vary the logarithmic slopes of the mass functions through the parameter  $\Delta\alpha$  around the  $\Lambda\text{CDM}$  prediction  $\Delta\alpha = 0$ . The parameters  $\beta$  and  $c_8$  set the logarithmic slope and amplitude of the concentration-mass relation, respectively. Black contours in the joint distributions show the 68% confidence region, and a black point identifies the  $\Lambda\text{CDM}$  prediction for each parameter, with the exception of  $\Sigma_{\text{sub}}$  (see main text).

density, particularly at the edge of the prior, but not by an amount that significantly affects our results<sup>10</sup>.

While we cannot constrain  $\Sigma_{\text{sub}}$  independently from the other parameters in  $\mathbf{q}_s$ , we can introduce a theoretically motivated prior that couples the amplitude of the subhalo mass

<sup>10</sup> In particular, the bin closest to  $\Sigma_{\text{sub}} = 0$  and  $\delta_{\text{LOS}} = 0$  does not actually contain zero halos, as it includes models with low amplitudes for both  $\Sigma_{\text{sub}}$  and  $\delta_{\text{LOS}}$ . These models require extremely high concentration parameters  $c_8$  to explain the data.

function,  $\Sigma_{\text{sub}}$ , to the amplitude of the line of sight halo mass function,  $\delta_{\text{LOS}}$ , at the pivot scale of  $10^8 M_\odot$ . As subhalos are accreted from the field, we expect that a universe with more (fewer)  $10^8 M_\odot$  halos in the field should have more (fewer) subhalos with an infall mass of  $10^8 M_\odot$ . Given an expected subhalo mass function amplitude<sup>11</sup>  $\Sigma_{\text{sub}(\text{predicted})}$  in

<sup>11</sup> We factor the redshift evolution and host halo mass dependence out of the normalization  $\Sigma_{\text{sub}}$ , so we expect a common value for all of the lenses deflectors in our sample.

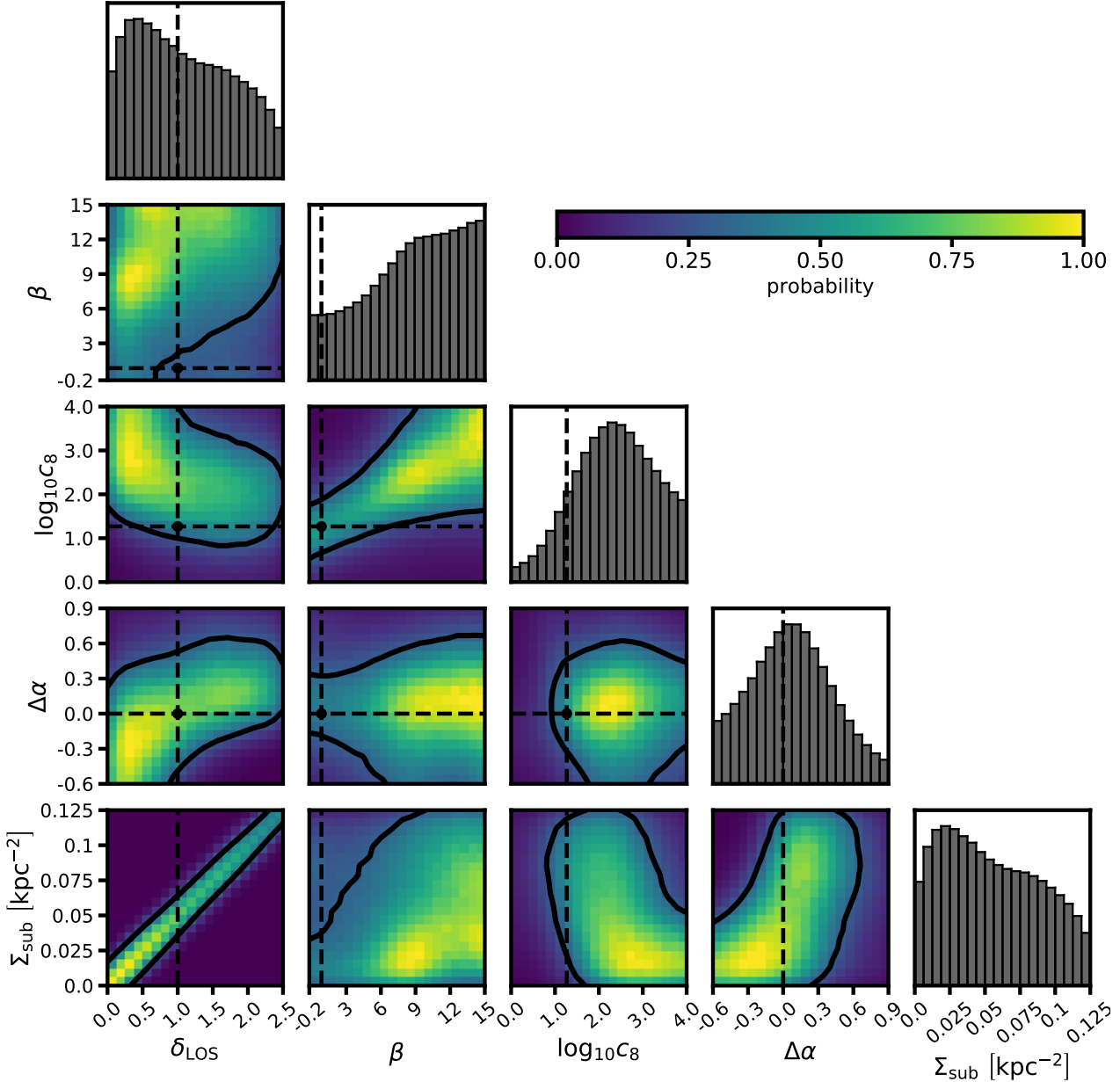


**Figure 4.** The joint probability distribution  $p(\Sigma_{\text{sub}}, \delta_{\text{LOS}}) \times p(\mathbf{q}_s | \mathcal{D})$ , where the first term is an informative prior on the combination of the normalization of the subhalo mass function and the field halo mass function. The prior couples the amplitudes of the field halo and subhalo mass functions such that they vary proportionally, reflecting the assumption that subhalos are accreted from the field. We assume a subhalo mass function amplitude  $\Sigma_{\text{sub}(\text{predicted})} = 0.05 \text{ kpc}^{-2}$ , which corresponds to twice as efficient tidal disruption of halos in the Milky Way relative to massive elliptical galaxies. We repeat the inference assuming  $\Sigma_{\text{sub}(\text{predicted})} = 0.025 \text{ kpc}^{-2}$  in Appendix C. Black contours in the joint distributions show the 68% confidence region, and a black point identifies the  $\Lambda\text{CDM}$  prediction for each parameter.

$\Lambda\text{CDM}$ , we define the relative excess or deficit of subhalos  $\delta\Sigma \equiv \Sigma_{\text{sub}}/\Sigma_{\text{sub}(\text{predicted})}$ , and demand that this relative excess or deficit vary proportionally with the relative excess or deficit of line-of-sight halos around the Sheth-Tormen prediction  $\delta_{\text{LOS}} = 1$ . We enforce this prior by adding importance sampling weights  $w \equiv p(\Sigma_{\text{sub}}, \delta_{\text{LOS}})$  given by

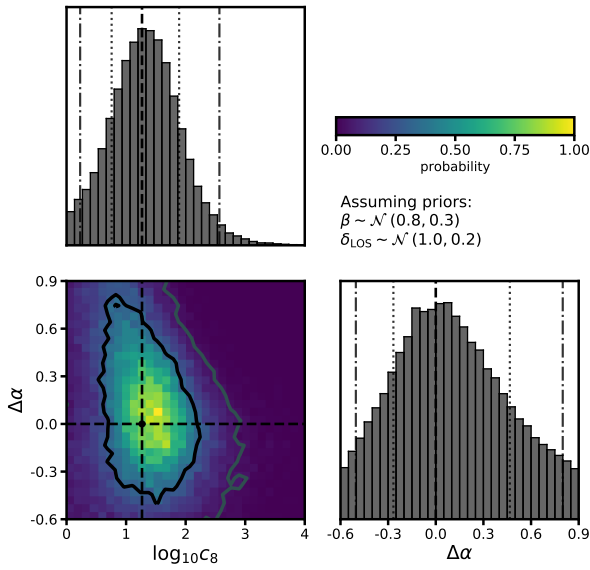
$$w = \exp\left(\frac{-(\delta\Sigma - \delta_{\text{LOS}})^2}{2\delta\Sigma^2}\right). \quad (16)$$

To be clear, we do not anchor the amplitudes of  $\Sigma_{\text{sub}}$  and  $\delta_{\text{LOS}}$  on small scales, which would trivially bring the inferred  $P(k)$  into agreement with theoretical expectations. The total number of subhalos and line of sight halos can still vary freely within the bounds of the chosen priors (see Table 2).

Assuming that massive elliptical galaxies and the Milky Way tidally disrupt subhalos with equal efficiency, we would expect an amplitude  $\Sigma_{\text{sub}(\text{predicted})} \sim 0.025 \text{ kpc}^{-2}$  for a universe with  $n_s = 0.9645$ ,  $a_{\text{run}} = 0$ , and  $b_{\text{run}} = 0$ , as shown

**Table 1.** The notation for several quantities that appear frequently in the text.

notation	description
$P(k)$	the primordial matter power spectrum
$P_{\Lambda\text{CDM}}$	a power spectrum given by $P(k_0) \left(\frac{k}{k_0}\right)^{-0.9645}$ with the amplitude $P(k_0)$ anchored by measurements on large scales
$\mathbf{q}_s$	hyper-parameters sampled in the lensing analysis, including $\Sigma_{\text{sub}}$ , $\delta_{\text{LOS}}$ , $\Delta\alpha$ , $c_8$ , and $\beta$
$\mathbf{q}_p$	parameters describing $P(k)$ beyond the pivot scale at $1 \text{ Mpc}^{-1}$ , including $n_s$ , $a_{\text{run}}$ , and $b_{\text{run}}$
$p(\mathbf{q}_s \mathbf{D})$	posterior distribution of $\mathbf{q}_s$ given the data $\mathbf{D}$
$p(\mathbf{q}_p \mathbf{D})$	posterior distribution of $\mathbf{q}_p$ given the data $\mathbf{D}$
$P_k$	the power spectrum $P(k)$ evaluated at some scale $k$
$\tilde{p}(P_k \mathbf{D})$	posterior distribution of $P_k$ given the data, assuming a uniform prior on $\mathbf{q}_p$
$p(P_k \mathbf{D})$	posterior distribution of $P_k$ given the data, assuming a log-uniform prior on $P_k$

**Figure 5.**

Joint inference of the amplitude of the concentration-mass relation at  $10^8 M_\odot$ ,  $c_8$ , and deviations of the logarithmic slope of the halo mass function  $\Delta\alpha$ , with the  $\Lambda\text{CDM}$  predictions highlighted with the black cross hairs and vertical dashed lines. Other vertical lines and contours denote 68% and 95% confidence intervals. We obtain this inference by multiplying the joint distribution shown in Figure 3 by a prior that enforces the  $\Lambda\text{CDM}$  prediction for the amplitude of the halo mass function  $\delta_{\text{LOS}} = 1 \pm 0.2$  and  $\beta = 0.8 \pm 0.3$ , while marginalizing over  $\Sigma_{\text{sub}}$ .

by Nadler et al. (2021). We expect, however, that the Milky Way's disk destroy subhalos more efficiently than an elliptical galaxy. Observational support for this assumption comes from Nadler et al. (2021), who find that a differential tidal disruption efficiency of  $\sim 2$  appears more consistent with the number of satellite galaxies in the Milky Way.

Taking these considerations into account, in the following sections we assume a value of  $\Sigma_{\text{sub(predicted)}} = 0.05 \text{ kpc}^{-2}$ , and couple the normalizations with  $\delta_\Sigma = 0.2$ , or a 20% intrinsic scatter between the amplitudes of the field halo and subhalo mass functions that could arise from halo to halo variance (Jiang & van den Bosch 2017). Figure 4 shows the resulting joint distribution of  $w \times p(\delta_{\text{LOS}}, \beta, \log_{10} c_8, \Delta\alpha | \mathbf{D})$ . In Appendix C, we perform our analysis assuming  $\Sigma_{\text{sub(predicted)}} = 0.025 \text{ kpc}^{-2}$ , and show that the effect of assuming a different value for  $\Sigma_{\text{sub(predicted)}}$  has a smaller affect on our results than the statistical uncertainty of our measurement.

As Figures 3 and 4 clearly demonstrate, the  $\Lambda\text{CDM}$  prediction lies within the 68% confidence intervals, so our results agree with the predictions of  $\Lambda\text{CDM}$ . However, we can make the agreement more striking by assigning an informative prior to the logarithmic slope of the concentration-mass relation  $\beta$ , and the amplitude of the line of sight halo mass function  $\delta_{\text{LOS}}$ . Doing so, we obtain the joint distribution  $p(\beta, \delta_{\text{LOS}} | \Lambda\text{CDM}) \times p(\mathbf{q}_s | \mathbf{D})$ , where the first term corresponds to Gaussian priors on  $\beta$  and  $\delta_{\text{LOS}}$  of  $\mathcal{N}(0.8, 0.3)$  and  $\mathcal{N}(1.0, 0.2)$ , respectively. Figure 5 shows the resulting joint distribution of  $\Delta\alpha$  and  $\log_{10} c_8$ , marginalized over the uniform prior on  $\Sigma_{\text{sub}}$  (without the importance weights  $w$ ). We infer  $\log_{10} c_8 = 1.3_{-0.5}^{+0.6}$  and  $1.3_{-1.1}^{+1.3}$  at 68% and 95% confidence, respectively. We infer  $\Delta\alpha = 0.08_{-0.34}^{+0.41}$  at 68% confidence. Both results are in excellent agreement with the predictions of  $\Lambda\text{CDM}$ .

## 5.2 Recasting the lensing measurement in terms of $n_s$ , $a_r$ , and $b_r$

To recast our inference in terms of  $\mathbf{q}_p = (n_s, a_{\text{run}}, b_{\text{run}})$ , we establish a one-to-one mapping between  $\mathbf{q}_s$  and  $\mathbf{q}_p$ . Using the semi-analytic modeling software `galacticus`, we compute the theoretical predictions for the halo mass function and concentration-mass relation (we described this procedure in Section 3). Then, for each theoretically-predicted

**Table 2.** The parameters sampled in this analysis that describe the halo mass function and concentration-mass relation, and the primordial matter power spectrum.

parameter	description	prior
$\delta_{\text{LOS}}$	amplitude of the line of sight halo mass function at $10^8 M_{\odot}$ relative to Sheth-Tormen	$\mathcal{U}(0, 2.5)$
$\beta$	logarithmic slope of the concentration-mass relation pivoting around $10^8 M_{\odot}$	$\mathcal{U}(-0.2, 15)$
$c_8$	amplitude of the concentration-mass relation at $10^8 M_{\odot}$	$\log_{10} \mathcal{U}(0, 4)$
$\Delta\alpha$	modifies logarithmic slope of halo and subhalo mass functions pivoting around $10^8 M_{\odot}$	$\mathcal{U}(-0.6, 0.9)$
$q$	couples the logarithmic slopes of the subhalo and field halo mass functions	$\mathcal{U}(0.7, 1.0)$
$\Sigma_{\text{sub}} [\text{kpc}^{-2}]$	subhalo mass function amplitude at $10^8 M_{\odot}$	$\mathcal{U}(0, 0.125)$
$\alpha$	CDM prediction for the logarithmic slope of the subhalo mass function pivoting around $10^8 M_{\odot}$	$\mathcal{U}(-1.95, -1.85)$
$n_s$	spectral index of $P(k)$ at $k > 1 \text{ Mpc}^{-1}$	$\mathcal{U}(0.3645, 1.5645)$
$a_{\text{run}}$	running of the spectral index at $k > 1 \text{ Mpc}^{-1}$	$\mathcal{U}(-0.2, 0.2)$
$b_{\text{run}}$	running of the running of the spectral index	$\mathcal{U}(-0.018, 0.018)$
$\sigma_{\text{src}} [\text{pc}]$	background source size nuclear narrow-line emission radio emission	$\mathcal{U}(25, 60)$ $\mathcal{U}(1, 20)$
$\gamma_{\text{macro}}$	logarithmic slope of main deflector mass profile	$\mathcal{U}(1.9, 2.2)$
$\gamma_{\text{ext}}$	external shear across main lens plane	(lens specific)
$a_4$	boxyness/diskyness of main deflector mass profile	$\mathcal{N}(0, 0.01)$

mass function and concentration-mass relation, we determine the set of  $\mathbf{q}_s$  parameters that minimize the residuals between the theoretical prediction and the model in terms of  $\mathbf{q}_s$ .

The dashed lines in Figure 2 show the best-fit model prediction for the halo mass function in terms of  $\delta_{\text{LOS}}$  and  $\Delta\alpha$  using Equation 11, and the best-fit concentration-mass relation parameterized in terms of  $c_8$  and  $\beta$  with Equation 13. The models we implemented for the lensing analysis accurately reproduce the theoretical predictions for most of the  $\mathbf{q}_p$  parameter space we consider, with a slight disagreement in the concentration-mass relation for large  $a_{\text{run}}$  and  $b_{\text{run}}$ . We assess how much this agreement affects our results in Appendix A, where we quantify potential sources of systematic error in our analysis.

To compute a corresponding set of  $\mathbf{q}_s$  parameters for any  $\mathbf{q}_p$ , we compute the mapping between  $\mathbf{q}_s$  and  $\mathbf{q}_p$  for values of  $n_s$  between 0.3645 and 1.5645,  $a_{\text{run}}$  between -0.2 and 0.2, and  $b_{\text{run}}$  between -0.018 and 0.018. Using 5,000 unique combinations of  $\mathbf{q}_p$  parameters, we interpolate the mapping to establish a continuous transformation between  $\mathbf{q}_p$  and  $\mathbf{q}_s$ .

Figure 6 shows the correspondence between the two sets of parameters as a function of  $n_s$ ,  $a_{\text{run}}$ , and two values of  $b_{\text{run}}$ . The line style indicates the value of  $b_{\text{run}}$ , while the color of each curve indicates the value of  $a_{\text{run}}$ . The y-axis shows the value of each  $\mathbf{q}_s$  parameter as a function of  $n_s$ . As discussed in the opening paragraph of Section 3, increasing the amount of small-scale power leads to covariant changes in the mass function and concentration-mass relation. Increasing power raises the amplitude of the mass function at  $10^8 M_{\odot}$  and makes halos more concentrated. Decreasing power makes halos less concentrated, lowers the amplitude at  $10^8 M_{\odot}$ , and leads to a shallower halo mass function slope (positive  $\Delta\alpha$ ).

Figure 6 shows the mapping calibrated using the Sheth-Tormen model for the halo mass function. As discussed in Section 3, we have also performed the analysis using two other models for the halo mass function. The other mass function models express similar trends between the  $\mathbf{q}_p$  and  $\mathbf{q}_s$  parameters, although they predict slightly higher mass function amplitudes  $\delta_{\text{los}}$ . In Appendix B, we repeat the analysis presented in this section using the other models for the halo mass function, and show that the statistical measure-

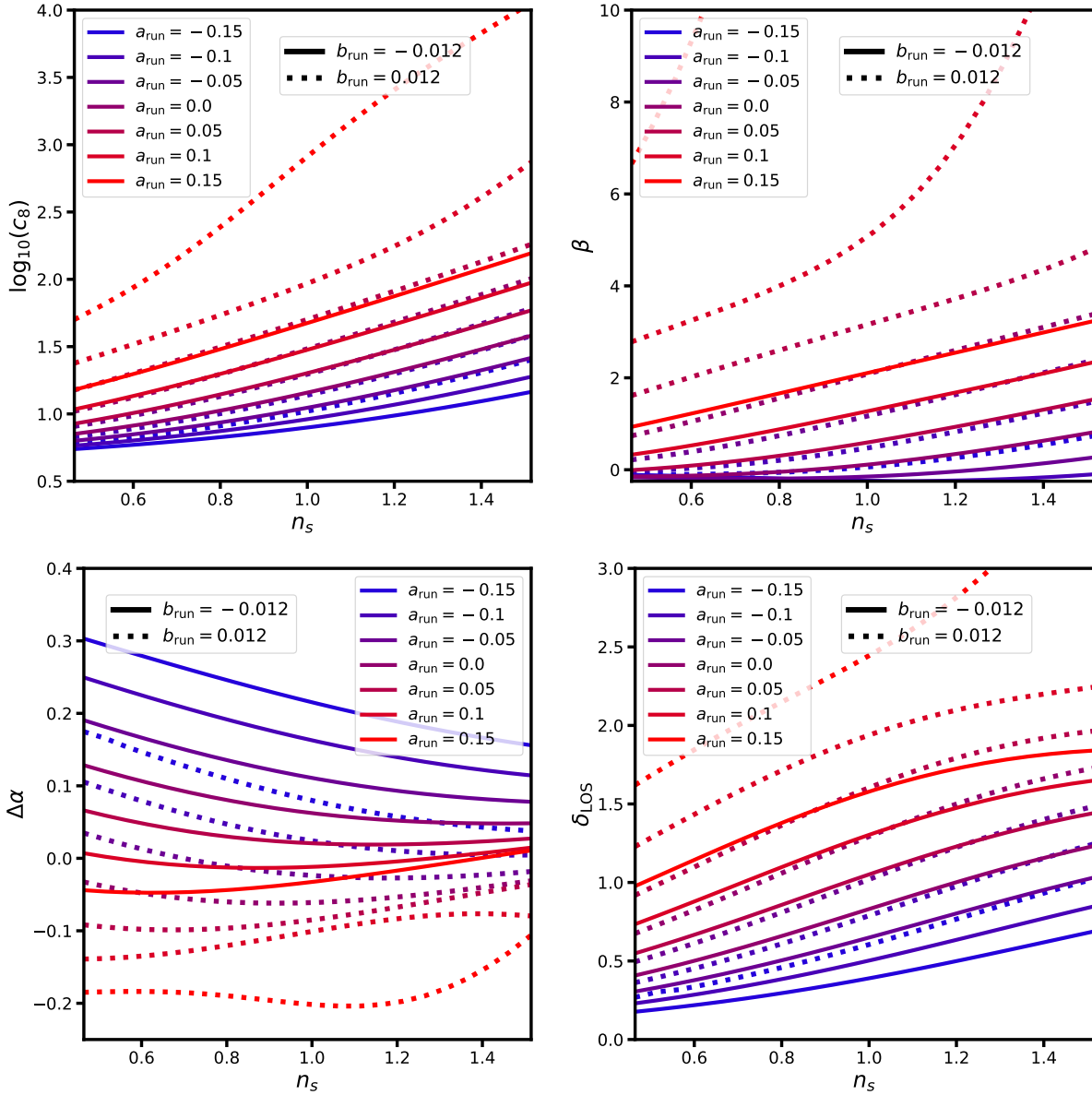


**Figure 6.** The correspondence between the hyper-parameters sampled in the lensing analysis  $\mathbf{q}_s$ , and the parameters in  $\mathbf{q}_p$ ,  $n_s$ ,  $a_{\text{run}}$ , and  $b_{\text{run}}$ , that determine the form of  $P(k)$ . The dashed and solid lines show the mapping  $\mathbf{q}_p \rightarrow \mathbf{q}_s$  for values of  $b_{\text{run}} = -0.012$  and  $b_{\text{run}} = 0.012$ , respectively. The color of each curve corresponds to the value of  $a_{\text{run}}$ , and the x-axis shows the value of  $n_s$ . The y-axis indicates the value of parameters in  $\mathbf{q}_s$  that corresponds to each form of the power spectrum.

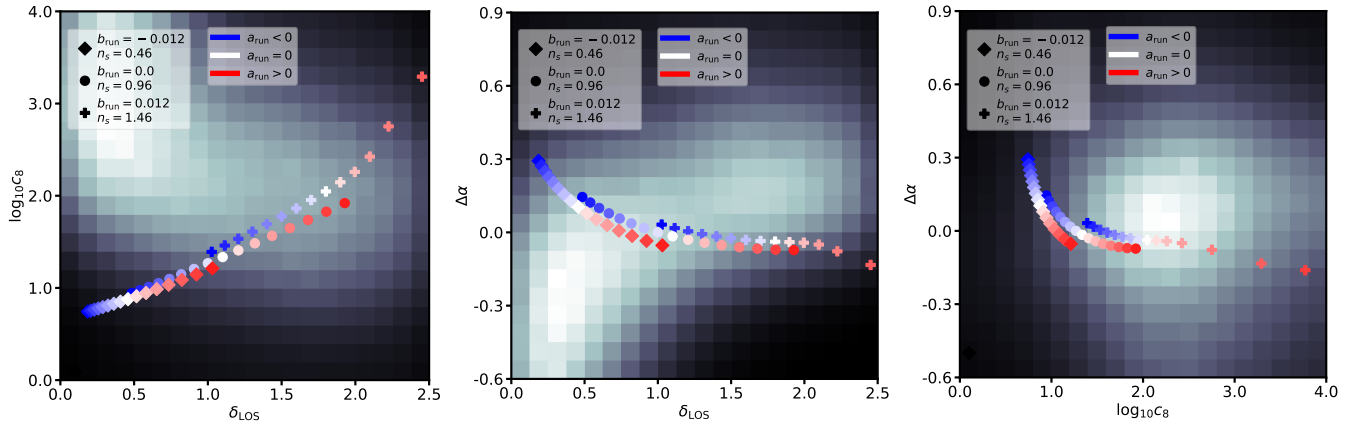
ment uncertainties are larger than the effect of using a different model for the halo mass function.

Figure 7 illustrates how the  $\mathbf{q}_p$  map to the likelihood obtained from the lensing analysis described in Section 5.1. Each figure shows a joint likelihood between  $\mathbf{q}_s$  parameters overlaid with three curves differentiated by the marker style. Diamonds indicate power spectrum models with suppressed small scale power, with  $b_{\text{run}} = -0.012$  and  $n_s = 0.46$ , crosses have enhanced small-scale power with  $b_{\text{run}} = 0.012$  and  $n_s = 1.46$ , and circles lie in between, with  $b_{\text{run}} = 0$  and  $n_s = 0.96$ . The color of each point indicates the value of  $a_{\text{run}}$ , with negative (positive) values of  $a_{\text{run}}$  corresponding to blue (red) points. The figure clearly shows that an enhancement of small-scale power introduce through one parame-

ter can offset a suppression of small scale power introduced through another. Models with positive  $a_{\text{run}}$ , but suppressed small scale power through low  $n_s$  and negative  $b_{\text{run}}$ , map to similar regions of  $\mathbf{q}_s$  parameter space<sup>12</sup>, and hence have roughly equal likelihoods, as models with negative  $a_{\text{run}}$ , and enhanced small-scale power through large  $n_s$  and positive  $b_{\text{run}}$ . We therefore expect anti-correlations between pairs of  $\mathbf{q}_p$  parameters.

Figure 7 also demonstrates why we can constrain  $P(k)$  using strong lensing data, even though the lensing infer-

<sup>12</sup> For example, the reddest diamond, which has  $b_{\text{run}} = -0.012$ ,  $n_s = 0.46$ , and  $a_{\text{run}} = 0.15$ , has a similar likelihood as the bluest cross, which has  $b_{\text{run}} = 0.12$ ,  $n_s = 1.46$ , and  $a_{\text{run}} = -0.15$ .



**Figure 7.** This figure shows points corresponding to different power spectra overlaid on the joint likelihood of several parameters sampled in the lensing analysis. The color of the points corresponds to the amplitude of  $a_{\text{run}}$  sampled between  $-0.1$  and  $0.1$ , while the marker style indicates values of  $b_{\text{run}}$  and  $n_s$ . First, we note that the likelihood contours inferred from the lenses, particularly in the left and center panels, run orthogonal to the relationship between model parameters that results from adding or reducing small-scale power. For this reason, we can constrain the form of the power spectrum without a statistically significant marginal constraint on any single parameter analyzed in the lensing analysis. Second, we note that models with reduced small-scale power introduced through  $b_{\text{run}} = -0.012$  and  $n_s = 0.46$ , but enhanced small scale power through  $a_{\text{run}}$ , map to similar regions of parameter space as models with enhanced small scale power through  $b_{\text{run}} = 0.012$  and  $n_s = 1.46$ , but negative values of  $a_{\text{run}}$ . Thus, we expect the joint probability distribution  $p(\mathbf{q}_p | \mathbf{D})$  to exhibit an anti-correlation between each pair of  $\mathbf{q}_p$  parameters.

ence itself exhibits significant covariance between model parameters that precludes statistically significant marginalized constraints on their values. Intuitively, our lensing inference identifies a volume of parameters space in  $\mathbf{q}_s$  that predicts a constant amount of magnification perturbation in the data. Simultaneously increasing the number of halos and their concentrations increases the amount of perturbation to image magnifications. Conversely, simultaneously lowering the amplitude of the mass function, and making halos less concentrated, reduces the amount of perturbation. To reproduce the amount of perturbation as in the data, strong lensing inferences therefore exhibit an anti-correlation between the amplitude of the halo mass function and the concentration-mass relation. Recalling the discussion in opening paragraph of Section 3 related to how altering the power spectrum at a scale  $\tilde{k}$  affects dark matter structure, we recall that increasing the amount of power at some scale  $\tilde{k}$  simultaneously increases the concentration and abundance of halos with mass  $\tilde{m}$ . As Figure 7 illustrates, the positive correlation between halo abundance and concentration that results from altering  $P(k)$  runs orthogonal to the anti-correlation between halo abundance and concentration allowed by the data, leading to constraints on the amplitude of  $P(k)$  from above and below.

### 5.3 Reconstructing the primordial matter power spectrum

We use the mapping between  $\mathbf{q}_p$  and  $\mathbf{q}_s$  to compute the joint distribution  $p(\mathbf{q}_p | \mathbf{D})$ . First, we generate 20,000 samples of  $\mathbf{q}_p$  from uniform priors on  $n_s$ ,  $a_{\text{run}}$ , and  $b_{\text{run}}$  in the ranges indicated in Table 2. Then, we assign each sample a likelihood by mapping each  $\mathbf{q}_p$  point to the corresponding point in the space of  $\mathbf{q}_s$ , and evaluate the probability of the  $\mathbf{q}_s$  point using the likelihood in Figure 4. Figure 8 shows the resulting joint distribution  $p(\mathbf{q}_p | \mathbf{D})$ . We recover the ex-

pected anti-correlation between  $\mathbf{q}_p$  parameters, as discussed in the previous section, and rule out simultaneously high or low values of  $n_s$ ,  $a_{\text{run}}$ , and  $b_{\text{run}}$ . We note that the prior we assign to  $\mathbf{q}_s$  parameters does not affect our inference on  $\mathbf{q}_p$ , because the relative likelihood between two points in  $\mathbf{q}_s$  parameter space, the only piece of information required to compute the probability distribution  $p(\mathbf{q}_p | \mathbf{D})$ , does not depend on the  $\mathbf{q}_s$  prior.

By sampling  $\mathbf{q}_p$  parameters from the joint distribution  $p(\mathbf{q}_p | \mathbf{D})$  and evaluating Equation 9, we can compute the posterior distribution  $\tilde{p}(P_k | \mathbf{D})$  of the power spectrum amplitude at any scale  $k$ , which we label  $P_k$ , given a uniform prior on  $n_s$ ,  $a_{\text{run}}$ , and  $b_{\text{run}}$ . However, a uniform prior on  $n_s$ ,  $a_{\text{run}}$ , and  $b_{\text{run}}$  does not correspond to a uniform prior on  $P_k$ . Rather, a uniform prior on  $\mathbf{q}_p$  parameters corresponds to an effective prior  $\pi_{\text{eff}}(P_k)$  for the power spectrum amplitude evaluated at  $k$ . When presenting our inference on the power spectrum at any scale throughout the remainder of this section, we divide the posterior distribution  $\tilde{p}(P_k | \mathbf{D})$  by this effective prior to obtain a new probability distribution  $p(P_k | \mathbf{D})$ , which has the interpretation of the posterior distribution of  $P_k$  given the data, assuming a log-uniform prior on  $P_k$ . Figure 9 shows the three distributions discussed in this paragraph - the posterior  $\tilde{p}(P_{25} | \mathbf{D})$ , the implicit prior  $\pi_{\text{eff}}(P_{25})$ , and the posterior distribution  $p(P_{25} | \mathbf{D})$ , evaluating the power spectrum model at  $k = 25 \text{ Mpc}^{-1}$ .

Using the likelihood  $p(\mathbf{q}_p | \mathbf{D})$ , we can reconstruct the shape of  $P(k)$ , assuming the model for the power spectrum given by Equation 9. The light gray curves in Figure 10 depict 20,000 individual power spectra that correspond to 20,000 samples of  $\mathbf{q}_p$  parameters drawn from the joint distribution  $p(\mathbf{q}_p | \mathbf{D})$ . The dark gray shaded region bounded by the black curves shows the 68% confidence interval of the distribution  $p(P_k | \mathbf{D})$  at each value of  $k$ . The inference obtained from the eleven lenses in our sample is consistent

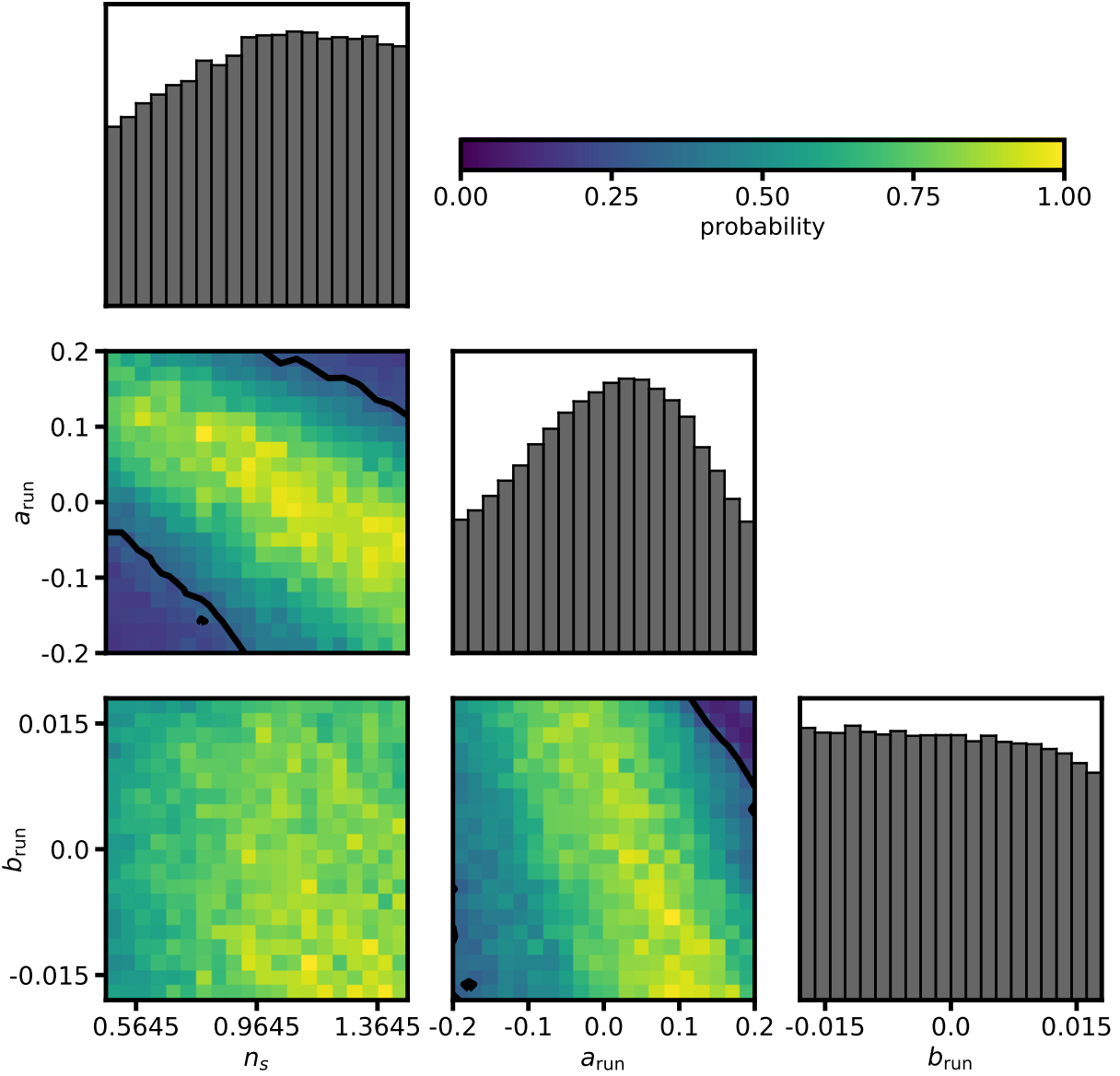


**Figure 8.** The posterior probability distribution  $p(\mathbf{q}_p | \mathcal{D})$ , obtained by mapping each point in the  $\mathbf{q}_p$  parameter space to the corresponding set of  $\mathbf{q}_s$  parameters, and evaluating the likelihood shown in Figure 4. Contours show 68% confidence intervals.

with the predictions of  $\Lambda$ CDM in the range of  $k$  values shown in the figure, between  $1 - 70 \text{ Mpc}^{-1}$ .

Typically, analyses of  $P(k)$  communicate results in terms of a constraint on the amplitude of  $P(k)$  in one or multiple  $k$  bins. Two aspects of our analysis complicate this method of presenting results. First, there is no obviously correct choice of  $k$  at which to evaluate Equation 9. Strong lensing probes dark matter structure in the mass range  $10^7 - 10^{10} M_\odot$ , corresponding to  $k$  scales ranging extending down to  $100 \text{ Mpc}^{-1}$ , but all scales in this range do not necessarily contribute to the measured signal in equal measure. Second, because we assume analytic model for  $P(k)$ , constraints on the amplitude at different  $k$  scales are not independent.

With these complications in mind, rather than quoting constraints at a particular scale, we quote constraints at three  $k$  scales probed by our data, and provide the covariance matrix between the inferences. We evaluate  $P(k)$  at  $k = 10, 25, \text{ and } 50 \text{ Mpc}^{-1}$ , where the largest  $k$  bin corresponds to a halo mass of roughly  $10^8 M_\odot$ . We identify this mass scale because strong lensing inferences on warm dark matter models rule out turnovers in the halo mass function below  $10^8 M_\odot$  (Gilman et al. 2020a), indicating the existing sample size of lenses can directly measure dark matter structure in this mass range. Relative to  $\Lambda$ CDM, we infer power spectrum amplitudes  $\log_{10}(P/P_{\Lambda\text{CDM}})$  of  $0.0^{+0.4}_{-0.4}$ ,  $0.1^{+0.6}_{-0.7}$ , and  $0.2^{+0.9}_{-1.0}$  at  $10, 25, \text{ and } 50 \text{ Mpc}^{-1}$ , in agreement with the predictions of  $\Lambda$ CDM and single-field slow-roll inflation.

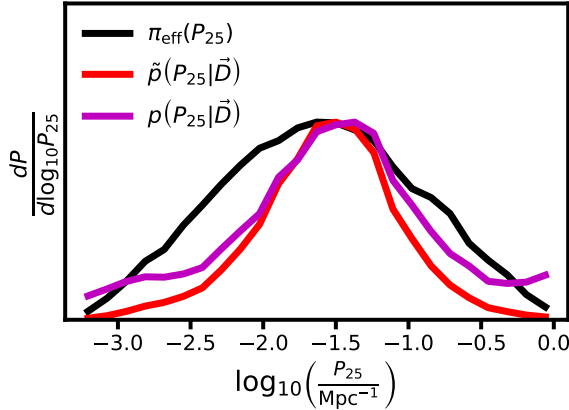


**Figure 9.** The effective prior  $\pi_{\text{eff}}(P_{25})$  on  $P_{25}$ , the power spectrum amplitude evaluated at  $25 \text{ Mpc}^{-1}$ , that corresponding to a uniform prior on  $\mathbf{q}_p$  parameters (black), the posterior distribution  $\tilde{p}(P_{25}|\mathbf{D})$  obtained from sampling the probability density shown in Figure 8 and evaluating Equation 9 (red), and the probability distribution  $p(\mathbf{q}_p|\mathbf{D}) \propto \frac{\tilde{p}(P_{25}|\mathbf{D})}{\pi_{\text{eff}}(P_{25})}$  (magenta). The magenta curve has the interpretation of the posterior distribution on  $P_{25}$  given the data, assuming a log-uniform prior on  $P_{25}$ . We use a value of  $k = 25 \text{ Mpc}^{-1}$  to create the figure, but this choice is arbitrary. When stating a constraint on the power spectrum amplitude at any scale (labeled  $P_k$ ), we follow the procedure illustrated in the figure to compute  $p(P_k|\mathbf{D})$ , and use this distribution to compute the median and confidence intervals.

We provide the covariance matrix for the power spectrum amplitude at different scales in Appendix D.

## 6 DISCUSSION

Using a sample of eleven quadruply-imaged quasars, we have performed a simultaneous inference of the halo mass function and the concentration-mass relation in the mass range  $10^7 - 10^{10} M_\odot$ , and cast the results in terms of the primordial matter power spectrum  $P(k)$  on length scales beyond the reach of existing measurements. We summarize our main results as follows:

- Assuming an analytic model for  $P(k)$  with a varying spectral index, running of the spectral index, and running-of-the-running beyond a pivot scale at  $1 \text{ Mpc}^{-1}$ , we constrain the form of the primordial matter power. Relative to  $P_{\Lambda\text{CDM}}$ , a model with no scale dependence of the spectral index, and with an amplitude anchored on large scales, we infer power spectrum amplitudes  $\log_{10}(P/P_{\Lambda\text{CDM}})$  at  $k = 10, 25$ , and  $50 \text{ Mpc}^{-1}$  of  $0.0^{+0.4}_{-0.4}, 0.1^{+0.6}_{-0.7}$ , and  $0.2^{+0.9}_{-1.0}$  at 68% confidence, in agreement with the predictions of  $\Lambda\text{CDM}$  and slow-roll inflation. Since we assume an analytic model for the power spectrum, the inferences on these scales are not independent. We provide covariance matrices for the measurements at the different scales in Appendix D.
- Assuming the  $\Lambda\text{CDM}$  prediction for the logarithmic slope of the concentration-mass relation and the amplitude of the halo mass function, we infer an amplitude  $c_8$  of the concentration-mass relation at  $10^8 M_\odot$  of  $\log_{10} c_8 = 1.3^{+0.6}_{-0.5}$  and  $1.3^{+1.3}_{-1.1}$  at 68% confidence and 95% confidence, respectively, and constrain deviations of the logarithmic slope of

the halo mass function around the  $\Lambda\text{CDM}$  prediction  $\Delta\alpha = 0$  to  $\Delta\alpha = 0.08^{+0.41}_{-0.34}$  at 68% confidence. These results are marginalized over the amplitude of the subhalo mass function, and are in excellent agreement with the predictions of  $\Lambda\text{CDM}$ .

The reach of strong lensing as a probe of fundamental physics extends beyond the confines of  $\Lambda\text{CDM}$  and warm dark matter, the two theoretical frameworks that typically underpin a strong lensing analysis and the interpretation of results. As we have demonstrated in this work, strong lensing of compact, unresolved sources can also constrain the initial conditions for structure formation quantified by the primordial matter power spectrum, which itself encodes properties of the inflaton. Our findings suggest that the small-scale behavior of the power spectrum does not significantly deviate from the power spectrum predicted by slow-roll inflationary models characterized by  $a_{\text{run}}$  and  $b_{\text{run}}$  of order  $|n_s - 1|$  and  $|n_s - 1|^2$ , respectively. Future analyses that build on the framework we present, utilizing a larger sample size of lenses and possibly refined calibrations of the halo mass function and concentration-mass relation, will enable tighter constraints on the abundance and concentration of low-mass dark matter halos, opening new avenues to constrain the properties of the early Universe.

As a necessary intermediate step in our analysis, we measured the abundance and concentrations of dark matter halos. In particular, assuming the  $\Lambda\text{CDM}$  prediction for the logarithmic slope of the concentration-mass relation and the amplitude of the field halo mass function, we obtained the tightest constraints on the amplitude of the concentration-mass relation and the slope of the halo mass function presented to date. The constraint on the concentration-mass relation is consistent with our previous work (Gilman et al. 2020b). Our measurement of the logarithmic slope of the halo mass function is consistent with the measurement presented by Vegetti et al. (2014), although our measurement reaches higher precision.

To date, strong lensing based inferences of alternatives to  $\Lambda\text{CDM}$  have focused on models of warm dark matter, characterized by a cutoff in the matter power spectrum and a suppression of small scale structure (Inoue et al. 2015; Birrer et al. 2017; Vegetti et al. 2018; Gilman et al. 2020a; Hsueh et al. 2020). Other analyses have sought to detect individual dark matter halos (Vegetti et al. 2014; Nierenberg et al. 2014; Hezaveh et al. 2016; Nierenberg et al. 2017; Çağan Sengül et al. 2021), or characterize general properties of the population of perturbing halos without attempting to distinguish between dark matter models (Dalal & Kochanek 2002; Gilman et al. 2020b). As we discuss in Section 5.2, the constraining power of strong lensing over  $P(k)$  comes from the joint distribution of mass function and concentration-mass relation amplitudes and logarithmic slopes. While some lensing analyses have constrained the mass function or concentration-mass relation independently of one another, no previous work has simultaneously measured these relations to account for covariance between them. For this reason, we cannot compare our results with previous lensing measurements in the context of power spectrum.

We have performed our analysis with three different models of the halo mass function (see Appendix B), and

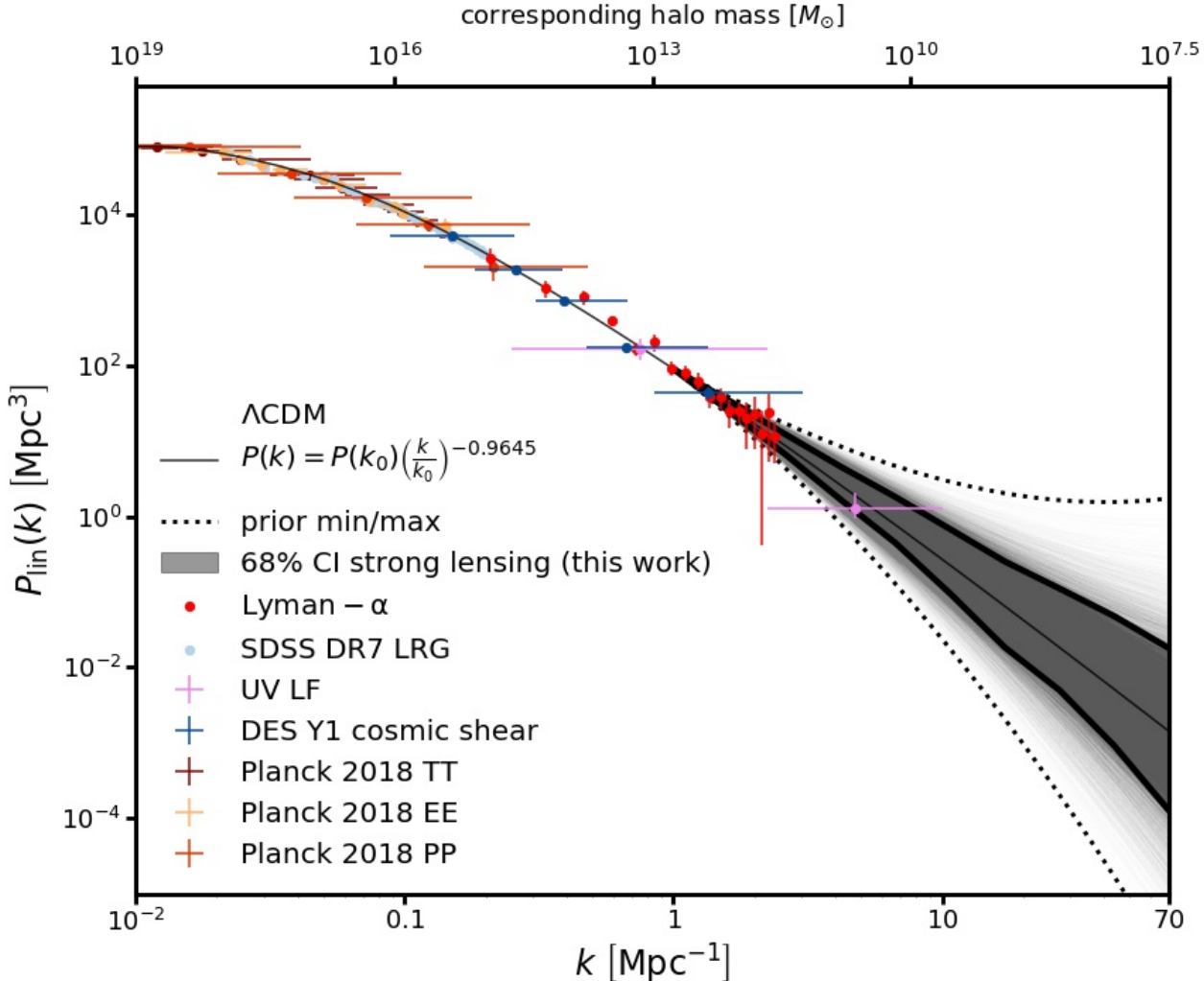


**Figure 10.** Measurements (colored points) and the  $\Lambda$ CDM prediction (black curve) for the matter power spectrum  $P_{\text{lin}} \equiv P(k) T^2(k)$ , where  $P(k)$  is the primordial matter power spectrum, and  $T(k)$  is the linear theory transfer function (Eisenstein & Hu 1998). Measurements shown in the figure come from analyses of CMB from the Planck satellite (Planck Collaboration et al. 2020a), galaxy clustering measured by the Dark Energy Survey (DES) (Troxel et al. 2018) and the Sloan Digital Sky Survey (SDSS) (Reid et al. 2010), the Lyman- $\alpha$  forest (Viel et al. 2004; Chabanier et al. 2019), and the ultra-violet luminosity function of distant galaxies (Sabti et al. 2021, with label UV LF). The lower x-axis shows the wavenumber  $k$ , and the upper axis shows a corresponding halo mass scale  $m = (4\pi/3)\rho_m(2\pi/k)^3$  computed with respect to the contribution of matter to the critical density of the Universe  $\rho_m$ . The light gray curves show 20,000 individual realizations of the power spectrum obtained by sampling the likelihood shown in Figure 8, and evaluating Equation 9. The dark gray band enclosed by the thick black curves shows the 68% confidence intervals of the power spectrum amplitude at each value of  $k$  sampled from  $p(P_k | \mathbf{D})$  (see the discussion in the caption of Figure 9). The upper and lower dashed black curves show the maximum and minimum power spectrum amplitude allowed by our model at each  $k$  scale, assuming the uniform priors on the parameters describing  $P(k)$  summarized in Table 2. We adapted this figure from Chabanier et al. (2019), using data products presented by Planck Collaboration et al. (2020a).

find that using a different model to connect the mass function to the power spectrum leads to shifts in our results by less than one standard deviation. However, as the sample size of lenses suitable for this analysis grows with forthcoming surveys and the James Webb Space telescope, the constraining power of strong lensing over the primordial matter power spectrum will grow. As the information content of the dataset expands, systematic uncertainties associated with the halo mass function and concentration-mass relation will become comparable with the statistical measurement uncertainties, and we will likely require a refined model for the halo mass function (e.g. Stafford et al. 2020; Brown et al.

2020; Ondaro-Mallea et al. 2021) that is calibrated in the mass and redshift range relevant for a strong lensing analysis,  $10^6 - 10^{10} M_\odot$  and  $z = 0 - 3$ , respectively.

Two practical considerations motivated our use of analytic model for  $P(k)$ . First, in order to compute the concentration-mass relation and halo mass function, we must be able to integrate and differentiate the power spectrum. A free-form model, in which the amplitude varies freely in separate  $k$  bins, would cause problems in the computation of the mass function and concentration-mass relation, unless the  $k$  bins become extremely narrow and approach a continuous representation of the power spec-

trum at different scales. Second, our strategy for constraining  $P(k)$  involves an intermediate measurement of several hyper-parameters  $\mathbf{q}_s$ , which we must then connect with a separate set of parameters that specify the form of the power spectrum. One advantage of this approach is that we can use different halo mass function and concentration-mass relation models to map  $\mathbf{q}_s \rightarrow \mathbf{q}_p$ . The price we pay for this flexibility is that we must restrict our analysis to models of  $P(k)$  that predict halo mass functions and concentration-mass relations that we can fit using our parameterization in terms of  $\mathbf{q}_s$ . In other words, we must restrict our analysis to models of  $P(k)$  where the concentration-mass relation is approximately given by a power law in peak height, and the where the halo mass function resembles a re-scaled version of Sheth-Tormen with a different logarithmic slope. An emulator that rapidly maps an arbitrary form for the power spectrum into a halo mass function and concentration-mass relation, effectively performing the forward modeling of observables directly on the level of the power spectrum, would allow us to explore a wider variety of forms for  $P(k)$ , facilitating more direct contact between strong lensing data and the properties of the early Universe.

## ACKNOWLEDGMENTS

We thank Krishna Choudhary, David Gilman, and Prateek Puri for comments on a draft version of this paper. DG was partially supported by a HQP grant from the McDonald Institute (reference number HQP 2019-4-2). DG and JB acknowledge financial support from NSERC (funding reference number RGPIN-2020-04712). AJB was supported in part by the NASA Astrophysics Theory Program, under grant 80NSSC18K1014. Support for this work was also provided by the National Science Foundation (NSF) through NSF AST-1716527. TT acknowledges support by NSF through grant AST-1714953, and grant AST-1836016, by NASA through and HST-GO-15652, by the Packard Foundation through a Packard Research Fellowship, and by the Moore Foundation through grant 8548.

We used three computing clusters to perform the ray-tracing simulations discussed in this paper. First, we used the Niagara supercomputer at the SciNet HPC Consortium with support provided by: the Canada Foundation for Innovation; the Government of Ontario; Ontario Research Fund - Research Excellence; and the University of Toronto. Second, we used computational and storage services associated with the Hoffman2 Shared Cluster provided by the UCLA Institute for Digital Research and Education's Research Technology Group. Third, we used the `memex` compute cluster, a resource provided by the Carnegie Institution for Science.

## DATA AVAILABILITY

Data used in this article came from observing programs HST-GO-13732 and HST-GO-15177. The data and analysis scripts used to prepare this article can be accessed at the following github repository <https://github.com/dangilman/lenslikelihood>.

## REFERENCES

Albrecht A., Steinhardt P. J., 1982, *Phys. Rev. Lett.*, 48, 1220  
 Amorisco N. C., et al., 2021, arXiv e-prints, p. arXiv:2109.00018  
 Astropy Collaboration et al., 2018, *AJ*, 156, 123  
 Auger M. W., Treu T., Bolton A. S., Gavazzi R., Koopmans L. V. E., Marshall P. J., Moustakas L. A., Burles S., 2010, *ApJ*, 724, 511  
 Baltz E. A., Marshall P., Oguri M., 2009, *JCAP*, 2009, 015  
 Bardeen J. M., Steinhardt P. J., Turner M. S., 1983, *Phys. RevD*, 28, 679  
 Bender R., Surma P., Doebeleiner S., Moellenhoff C., Madejsky R., 1989, *AA*, 217, 35  
 Benson A. J., 2012, *NewA*, 17, 175  
 Bhattacharya S., Heitmann K., White M., Lukić Z., Wagner C., Habib S., 2011, *ApJ*, 732, 122  
 Birrer S., Amara A., 2018, *Physics of the Dark Universe*, 22, 189  
 Birrer S., Amara A., Refregier A., 2017, *JCAP*, 2017, 037  
 Birrer S., et al., 2021, *The Journal of Open Source Software*, 6, 3283  
 Blandford R., Narayan R., 1986, *ApJ*, 310, 568  
 Bode P., Ostriker J. P., Turok N., 2001, *ApJ*, 556, 93  
 Bohr S., Zavala J., Cyr-Racine F.-Y., Vogelsberger M., 2021, *MNRAS*, 506, 128  
 Brown S. T., McCarthy I. G., Diemer B., Font A. S., Stafford S. G., Pfeifer S., 2020, *MNRAS*, 495, 4994  
 Bullock J. S., Kolatt T. S., Sigad Y., Somerville R. S., Kravtsov A. V., Klypin A. A., Primack J. R., Dekel A., 2001, *MNRAS*, 321, 559  
 Chabanier S., Millea M., Palanque-Delabrouille N., 2019, *MNRAS*, 489, 2247  
 Chiba M., Minezaki T., Kashikawa N., Kataza H., Inoue K. T., 2005, *ApJ*, 627, 53  
 Chluba J., Erickcek A. L., Ben-Dayan I., 2012, *ApJ*, 758, 76  
 Dalal N., Kochanek C. S., 2002, *ApJ*, 572, 25  
 Despali G., Giocoli C., Angulo R. E., Tormen G., Sheth R. K., Baso G., Moscardini L., 2016, *MNRAS*, 456, 2486  
 Diemer B., 2018, *ApJS*, 239, 35  
 Diemer B., Joyce M., 2019, *ApJ*, 871, 168  
 Diemer B., More S., Kravtsov A. V., 2013, *ApJ*, 766, 25  
 Dobler G., Keeton C. R., 2006, *MNRAS*, 365, 1243  
 Eisenstein D. J., Hu W., 1998, *ApJ*, 496, 605  
 Eke V. R., Navarro J. F., Steinmetz M., 2001, *ApJ*, 554, 114  
 Fedeli C., Finelli F., Moscardini L., 2010, *MNRAS*, 407, 1842  
 Gilman D., Agnello A., Treu T., Keeton C. R., Nierenberg A. M., 2017, *MNRAS*, 467, 3970  
 Gilman D., Birrer S., Treu T., Keeton C. R., Nierenberg A., 2018, *MNRAS*, 481, 819  
 Gilman D., Birrer S., Treu T., Nierenberg A., Benson A., 2019, *MNRAS*, 487, 5721  
 Gilman D., Birrer S., Nierenberg A., Treu T., Du X., Benson A., 2020a, *MNRAS*, 491, 6077  
 Gilman D., Du X., Benson A., Birrer S., Nierenberg A., Treu T., 2020b, *MNRAS*, 492, L12  
 Gilman D., Bovy J., Treu T., Nierenberg A., Birrer S., Benson A., Sameie O., 2021, *MNRAS*, 507, 2432

Green S. B., van den Bosch F. C., 2019, MNRAS, 490, 2091  
 Guth A. H., 1981, PhysRevD, 23, 347  
 Guth A. H., Pi S. Y., 1982, Phys. Rev. Lett., 49, 1110  
 Hezaveh Y. D., et al., 2016, ApJ, 823, 37  
 Hinshaw G., et al., 2013, ApJS, 208, 19  
 Hsueh J. W., Fassnacht C. D., Vegetti S., McKean J. P., Spingola C., Auger M. W., Koopmans L. V. E., Lagattuta D. J., 2016, MNRAS, 463, L51  
 Hsueh J. W., et al., 2017, MNRAS, 469, 3713  
 Hsueh J.-W., Despali G., Vegetti S., Xu D., Fassnacht C. D., Metcalf R. B., 2018, MNRAS, 475, 2438  
 Hsueh J. W., Enzi W., Vegetti S., Auger M. W., Fassnacht C. D., Despali G., Koopmans L. V. E., McKean J. P., 2020, MNRAS, 492, 3047  
 Inoue K. T., Chiba M., 2005, ApJ, 634, 77  
 Inoue K. T., Takahashi R., Takahashi T., Ishiyama T., 2015, MNRAS, 448, 2704  
 Jiang F., van den Bosch F. C., 2017, MNRAS, 472, 657  
 Lazar A., Bullock J. S., Boylan-Kolchin M., Feldmann R., Çatmabacak O., Moustakas L., 2021, MNRAS, 502, 6064  
 Linde A. D., 1982, Physics Letters B, 108, 389  
 Minor Q., Kaplinghat M., Chan T. H., Simon E., 2021, MNRAS, 507, 1202  
 More S., Diemer B., Kravtsov A. V., 2015, ApJ, 810, 36  
 Müller-Sánchez F., Prieto M. A., Hicks E. K. S., Vives-Arias H., Davies R. I., Malkan M., Tacconi L. J., Genzel R., 2011, ApJ, 739, 69  
 Nadler E. O., Birrer S., Gilman D., Wechsler R. H., Du X., Benson A., Nierenberg A. M., Treu T., 2021, ApJ, 917, 7  
 Navarro J. F., Frenk C. S., White S. D. M., 1997, ApJ, 490, 493  
 Nierenberg A. M., Treu T., Wright S. A., Fassnacht C. D., Auger M. W., 2014, MNRAS, 442, 2434  
 Nierenberg A. M., et al., 2017, MNRAS, 471, 2224  
 Nierenberg A. M., et al., 2020, MNRAS, 492, 5314  
 Ondaro-Mallea L., Angulo R. E., Zennaro M., Contreras S., Aricò G., 2021, arXiv e-prints, p. arXiv:2102.08958  
 Planck Collaboration et al., 2014, AA, 571, A16  
 Planck Collaboration et al., 2020a, AA, 641, A1  
 Planck Collaboration et al., 2020b, AA, 641, A8  
 Planck Collaboration et al., 2020c, AA, 641, A10  
 Prada F., Klypin A. A., Cuesta A. J., Betancort-Rijo J. E., Primack J., 2012, MNRAS, 423, 3018  
 Press W. H., Schechter P., 1974, ApJ, 187, 425  
 Reid B. A., et al., 2010, MNRAS, 404, 60  
 Rodríguez-Puebla A., Behroozi P., Primack J., Klypin A., Lee C., Hellinger D., 2016, MNRAS, 462, 893  
 Rubin D. B., 1984, The Annals of Statistics, 12, 1151  
 Sabti N., Muñoz J. B., Blas D., 2021, arXiv e-prints, p. arXiv:2110.13161  
 Schneider A., Smith R. E., Macciò A. V., Moore B., 2012, MNRAS, 424, 684  
 Sheth R. K., Mo H. J., Tormen G., 2001, MNRAS, 323, 1  
 Springel V., et al., 2008, MNRAS, 391, 1685  
 Stacey H. R., Lafontaine A., McKean J. P., 2020, MNRAS, 493, 5290  
 Stafford S. G., Brown S. T., McCarthy I. G., Font A. S., Robertson A., Poole-McKenzie R., 2020, MNRAS, 497, 3809  
 Starobinsky A. A., 1982, Physics Letters B, 117, 175  
 Sugai H., Kawai A., Shimono A., Hattori T., Kosugi G., Kashikawa N., Inoue K. T., Chiba M., 2007, ApJ, 660, 1016  
 Tinker J., Kravtsov A. V., Klypin A., Abazajian K., Warren M., Yepes G., Gottlöber S., Holz D. E., 2008, ApJ, 688, 709  
 Troxel M. A., et al., 2018, PhysRevD, 98, 043528  
 Vegetti S., Koopmans L. V. E., Auger M. W., Treu T., Bolton A. S., 2014, MNRAS, 442, 2017  
 Vegetti S., Despali G., Lovell M. R., Enzi W., 2018, MNRAS, 481, 3661  
 Viel M., Weller J., Haehnelt M. G., 2004, MNRAS, 355, L23  
 Vogelsberger M., Zavala J., Cyr-Racine F.-Y., Pfrommer C., Bringmann T., Sigurdson K., 2016, MNRAS, 460, 1399  
 Wechsler R. H., Bullock J. S., Primack J. R., Kravtsov A. V., Dekel A., 2002, ApJ, 568, 52  
 Çağan Şengül A., Dvorkin C., Ostdiek B., Tsang A., 2021, arXiv e-prints, p. arXiv:2112.00749

## APPENDIX A: QUANTIFYING THE EFFECTS OF SYSTEMATIC MODELING UNCERTAINTIES

We identify two potential sources of systematic error in our analysis. The first relates to the theoretical models used to predict the mass function and concentration-mass relation. If the models break down for certain combinations of  $n_s$ ,  $a_{\text{run}}$  and  $b_{\text{run}}$ , then the predicted mass functions and concentration-mass relations will not have the correct dependence on the power spectrum parameters. To quantify the extent to which this occurs, if it occurs at all, will require targeted N-body simulations, and possibly a refinement of the model for halo mass function and the concentration-mass relation. Further investigation of how changes to the power spectrum affect dark matter structure, similar to the analyses carried out by (Brown et al. 2020; Ondaro-Mallea et al. 2021), can help address this issue, and potentially improve on the results we present.

The second source of systematic uncertainty relates to our strategy for connecting the parameters  $\delta_{\text{LOS}}$ ,  $\beta$ ,  $c_s$ , and  $\Delta\alpha$  to the power spectrum. If, for example, the concentration-mass relation deviates from a power-law in the peak height, or if the halo mass function deviates from a re-scaled version of the Sheth-Tormen mass function with a modified logarithmic slope, then our parameterization in terms of  $\beta$  and  $\Delta\alpha$  would not exactly describe the populations of dark matter halos that would exist for a given  $n_s$ ,  $a_{\text{run}}$  and  $b_{\text{run}}$ . The lower right panel of Figure 2 shows an example of this, as the theoretical prediction for the concentration-mass relation with  $b_{\text{run}} = 0.01$  and  $a_{\text{run}} = 0.14$  forms a curve with a positive second derivative in the logarithmic slope not captured by a power law in peak height (solid curve).

To account for uncertainties related to the logarithmic slopes in different mass ranges, we re-calibrate the mapping between  $\mathbf{q}_s$  and  $\mathbf{q}_p$  by fitting the mass function and concentration-mass relation in different mass ranges around the baseline range of  $10^7 - 10^9 M_\odot$ <sup>13</sup>. By computing best

<sup>13</sup> We identify this mass range as the most relevant for lensing

fit values of  $\beta$  and  $\Delta\alpha$  in the range  $10^7 - 10^8 M_\odot$  and  $10^8 - 10^9 M_\odot$ , we can estimate how much our results depend on the deviation of the logarithmic slope of the mass function and concentration-mass relation around the functional form assumed in our model. We define the systematic errors in  $\beta$  and  $\Delta\alpha$ , which we compute by fitting the mass function and concentration-mass relation in different mass ranges,  $\delta F_\beta$  and  $\delta F_{\Delta\alpha}$ , respectively. We compute these quantities as a function of  $n_s$ ,  $a_{\text{run}}$ , and  $b_{\text{run}}$ , so that we can estimate the systematic error for any point in the space of  $\mathbf{q}_p$  parameters.

By construction, the normalization parameters  $c_8$  and  $\delta_{\text{LOS}}$  are defined at a particular pivot scale of  $10^8 M_\odot$ , and therefore do not depend on the mass range where we establish the mapping from  $\mathbf{q}_s$  to  $\mathbf{q}_p$ . However, as we have modeled the mass function in the lensing analysis relative to Sheth-Tormen with  $n_s = 0.9645$ ,  $a_{\text{run}} = 0$ , and  $b_{\text{run}} = 0$ , we do not explicitly account for different redshift evolution of the mass function with the  $\mathbf{q}_p$  parameters. Similarly, the redshift evolution of the concentration-mass relation may also depend on  $\mathbf{q}_p$  in a manner that we do not explicitly include in the lensing measurement.

To assess the importance of these effects, we can estimate the systematic error associated with the redshift evolution of the halo mass function  $n(m, z, n_s, a_{\text{run}}, b_{\text{run}})$  by computing the absolute error in the redshift evolution as a function of the power spectrum parameters

$$\delta F_{\delta_{\text{LOS}}} \equiv \frac{n(10^8, z, n_s, a_{\text{run}}, b_{\text{run}})}{n(10^8, 0, n_s, a_{\text{run}}, b_{\text{run}})} - \frac{n(10^8, z, 0.9645, 0, 0)}{n(10^8, 0, 0.9645, 0, 0)}. \quad (\text{A1})$$

We use an analogous expression for the redshift evolution of the concentration-mass relation  $c(m, z, n_s, a_{\text{run}}, b_{\text{run}})$  to compute  $\delta F_{c_8}$ . Given that redshift range relevant for strong lensing is approximately  $z = 0 - 2$ , we evaluate the expressions for  $\delta F_{c_8}$  and  $\delta F_{\delta_{\text{LOS}}}$  at  $z = 1$ .

Figure A1 illustrates the effect of the aforementioned systematic errors in our analysis. The figure shows the inference of the power spectrum amplitude evaluated at  $25 \text{ Mpc}^{-1}$  (the exact  $k$  value where we compute the power is irrelevant for this discussion) for different perturbed mappings  $\mathbf{q}_p \rightarrow \mathbf{q}_s + \delta \mathbf{F}$ , where  $\delta \mathbf{F} \equiv (\delta F_{\delta_{\text{LOS}}}, \delta F_{c_8}, \delta F_{\Delta\alpha}, \delta F_\beta)$ . Each color denotes a different combination of systematics. Our results do not change significantly for two reasons: First, changes to the power spectrum result in order of magnitude changes in  $c_8$ , and much larger changes in  $\beta$  and  $\Delta\alpha$  than those associated with the systematic uncertainties in our model. Second, due to the relatively small sample size of eleven lenses, our statistical measurement uncertainties are large enough that we cannot constrain the model parameters at the level of the systematic errors. To obtain our main results, and when quoting an inference of  $P(k)$  at any scale, we have taken the average of the six probability distributions shown in Figure A1.

analyses with flux ratios given the sensitivity of the data determined by the background source size, and the masses and abundance of halos.

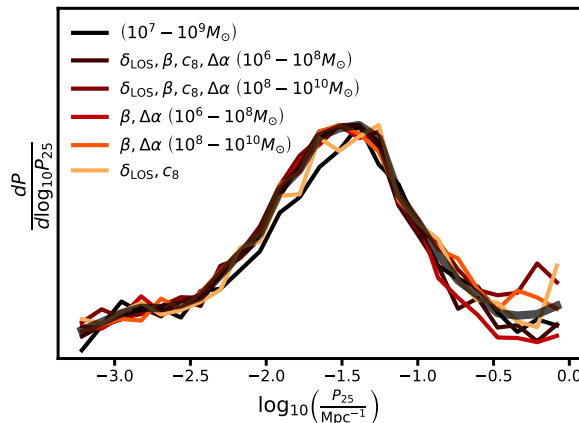


Figure A1.

An illustration of how systematic modeling uncertainties associated with the mapping between  $\mathbf{q}_p$  and  $\mathbf{q}_s$  parameters affect our main results. Each colored curve depicts an inference of  $P(k)$  at  $25 \text{ Mpc}^{-1}$  using an altered mapping  $\mathbf{q}_s \rightarrow \mathbf{q}_p + \delta \mathbf{q}_p$ , where  $\delta \mathbf{q}_p$  includes errors associated with the amplitudes and logarithmic slopes of the mass function and concentration-mass relation. The mass range in parenthesis indicates where we compute the mapping  $\mathbf{q}_p \rightarrow \mathbf{q}_s$ , which can impact the logarithmic slopes predicted by a particular set of  $n_s$ ,  $a_{\text{run}}$ , and  $b_{\text{run}}$ . We estimate the errors in the mass function amplitudes by performing the mapping to  $c_8$  and  $\delta_{\text{LOS}}$  at  $z = 1$ . The parameters listed in front of the mass range in parenthesis indicate which systematic errors are included in each curve. The medians and confidence intervals we present in Section 6 are computed by averaging the inferences together, shown in the figure as a thick black curve.

## APPENDIX B: RESULTS WITH DIFFERENT MASS FUNCTION MODELS AND PIVOT SCALES

### B1 Results with different mass functions

We consider two mass function models in addition to Sheth-Tormen that we use to connect the hyper-parameters sampled in the lensing analysis,  $\mathbf{q}_s$ , to the parameters describing the power spectrum,  $\mathbf{q}_p$ . First, we consider is the mass function model presented Rodriguez-Puebla et al. (2016, hereafter Rodriguez-Puebla). The Rodriguez-Puebla model used the same model for  $f(\sigma)$  as Tinker et al. (2008)

$$f(\sigma) = A \left[ \left( \frac{\sigma}{b} \right)^{-a} + 1 \right] \exp \left( \frac{-b}{\sigma^2} \right), \quad (\text{B1})$$

but the parameters  $a$  and  $b$  are re-calibrated to the Planck 2013 cosmology (Planck Collaboration et al. 2014) down to halo masses of  $\sim 10^{10} M_\odot$ , and redshifts  $z = 0 - 9$ .

In addition to Sheth-Tormen and Rodriguez-Puebla, we repeat our analysis using the model presented by Bhattacharya et al. (2011) (hereafter referred to as the Bhattacharya model). Bhattacharya et al. (2011) added an additional free parameter to make an empirical adjustment to the model for  $f(\sigma, z)$  in the Sheth-Tormen model. The additional term has the form  $\left( \frac{\delta_c \sqrt{a}}{\sigma} \right)^q$ , with the additional parameter  $q$  fit simultaneously with  $a$  and  $p$ . Bhattacharya et al. (2011) included the redshift evolution of the mass function is explicitly in their model in order to match simulations on mass scales above  $6 \times 10^{11} M_\odot$ , and  $z = 0 - 2$ .

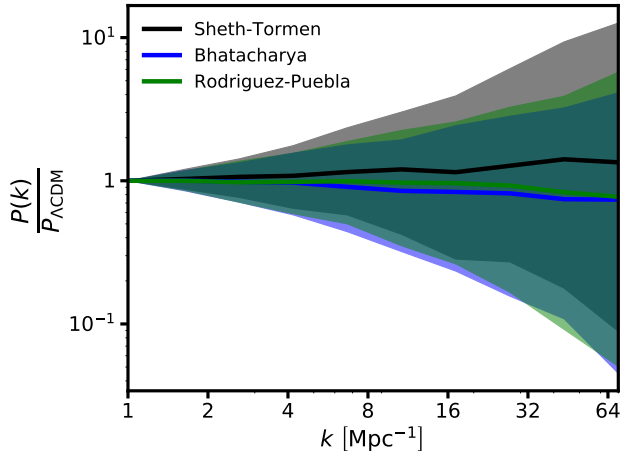


**Figure B1.**

The reconstructed primordial matter power spectrum using the mass function model presented by Bhattacharya et al. (2011) (blue) and Rodríguez-Puebla et al. (2016) (green) to connect the primordial matter power spectrum to abundance of dark matter halos, in comparison with the Sheth-Tormen model (black).

Both the Bhattacharya and Rodríguez-Puebla models predict a  $\sim 25\%$  higher mass function amplitude  $\delta_{\text{LOS}}$  than the Sheth-Tormen model, and very similar logarithmic slopes  $\Delta\alpha$ . The higher mass function amplitude introduces more halos into the lens models, which in turn enables in tighter constraints on the concentration-mass relation and the logarithmic slope. For this reason, our constraints on  $P(k)$  become stronger when using the Bhattacharya and Rodríguez-Puebla models. Figure B1 shows the power spectrum inference relative to the  $\Lambda\text{CDM}$  prediction obtained with the three mass function models we implemented.

## B2 Results with different pivot scales

There is no obvious ‘correct’ choice of pivot scale for our analysis, because our data probes roughly three orders of magnitude of halo mass, and structure at each corresponding  $k$  scale does not necessarily contribute in equal measure to the signal. We can only reason about an appropriate choice of pivot scale in general terms. At one extreme, putting the pivot at  $k_0 = 1000 \text{ Mpc}^{-1}$  would result in no constraints on  $P(k)$ , since the properties of dark matter halos we can detect remains unaffected. On the other extreme, placing the pivot at very large scales and varying  $q_p$  would violate well-established and precisely measured properties of the Universe on large scales. Somewhere in between these extremes lies the ‘optimal pivot’, although there is no clear method for determining it with the analysis tools at our disposal. We have attempted to find the choice of pivot scale that minimizes the uncertainties at different values of  $k$ , but see no clear trend that would justify one choice over another.

To explore what effect the pivot scale has on our results, we perform our analysis assuming the same power spectrum model as given by Equation 9, but with  $k_0 = 0.1 \text{ Mpc}^{-1}$ , and  $k_0 = 0.5 \text{ Mpc}^{-1}$ . The upper and lower panels in Figure B2 show the resulting power spectrum reconstructions, assuming the Sheth-Tormen mass function. Shifting the pivot to larger scales leads to a slight increase in the uncertainty

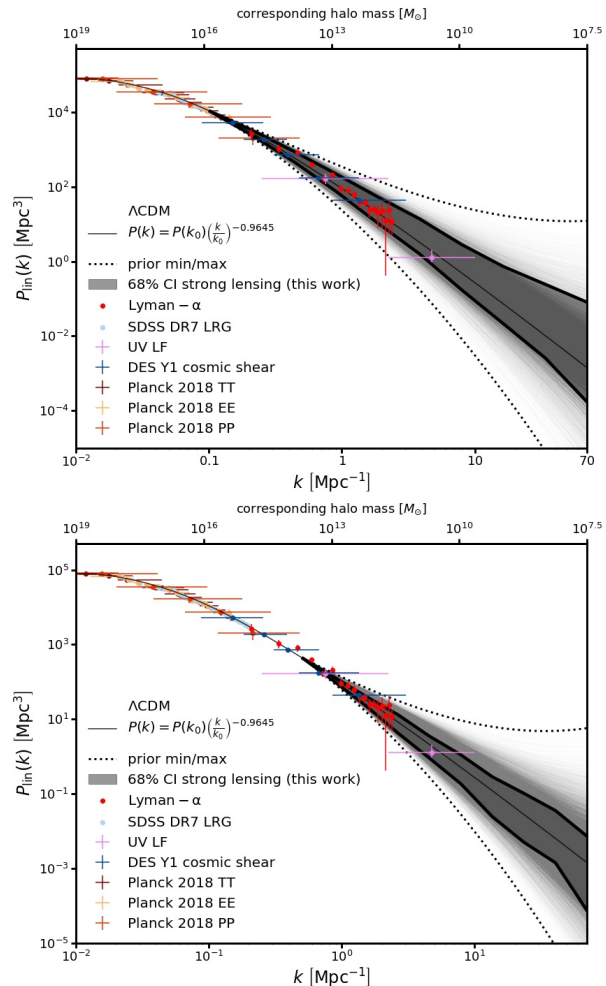


**Figure B2.** The reconstructed primordial matter power spectrum using the mass function model presented by Sheth et al. (2001) with a pivot scale  $k_0 = 0.1 \text{ Mpc}^{-1}$  (top) and  $k_0 = 0.5 \text{ Mpc}^{-1}$  (bottom).

of the power spectrum amplitude at smaller scales, but by much less than the statistical measurement uncertainty of our main result. As the choice does not significantly affect our results, we place the pivot at  $k_0 = 1 \text{ Mpc}^{-1}$  to isolate deviations on smaller scales while preserving the large-scale structure of the Universe. We also experimented with a pivot at  $5 \text{ Mpc}^{-1}$ . However, the resulting mass functions and concentration-mass relations had curvature that we could not accurately fit with the parameterization for these relations in terms of the  $q_s$  parameters.

## APPENDIX C: RESULTS WITH DIFFERENT COUPLING BETWEEN THE SUBHALO AND FIELD HALO MASS FUNCTIONS

The subhalo mass function grows by accretion of field halos, so we expect correlation between the logarithmic slopes of the field halo and subhalo mass function, and their amplitudes. We have explicitly included the coupling between the logarithmic slopes of the mass functions through the parameter  $\Delta\alpha$ . The amplitude of the subhalo mass func-

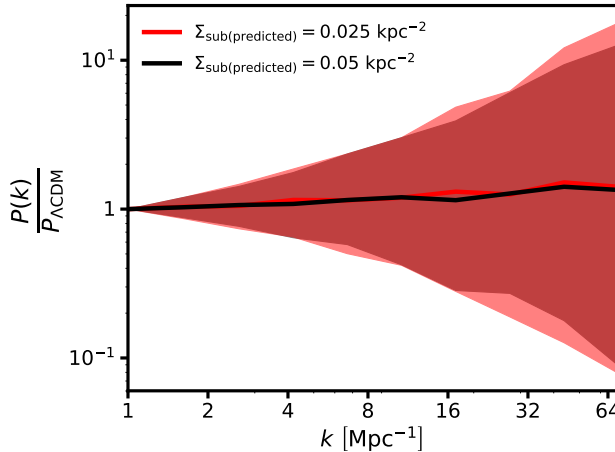


**Figure C1.**

The inference of the primordial matter power spectrum relative to the  $\Lambda$ CDM prediction assuming a subhalo mass function amplitude of  $\Sigma_{\text{sub(predicted)}} = 0.05 \text{ kpc}^{-1}$  (black) and  $\Sigma_{\text{sub(predicted)}} = 0.025 \text{ kpc}^{-1}$  (red).

tion, however, depends on how efficiently elliptical galaxies disrupt halos after accretion, and it is therefore subject to additional theoretical uncertainty.

We assume that the amplitude of the subhalo mass function varies proportionally with the amplitude of the field halo mass function. In terms of the parameters implemented in our analysis, an amplitude of the subhalo mass function  $\Sigma_{\text{sub(predicted)}}$  would correspond to the  $\Lambda$ CDM prediction for the amplitude of the field halo mass function  $\delta_{\text{LOS}} = 1.0$ . If the amplitude of the field halo mass function were 50% higher, we would therefore expect to measure  $\delta_{\text{LOS}} = 1.5$  and  $\sigma_{\text{sub}} = 1.5 \times \Sigma_{\text{sub(predicted)}}$ . As discussed in Section 5, we implement this assumption by adding importance weights  $w$  to the samples in the posterior distribution  $p(\mathbf{q}_s | \mathbf{D})$ .

Motivated by the results presented by Nadler et al. (2021), who compared strong lensing inferences of the subhalo mass function with measurements of Milky Way satellites, we assume a value  $\Sigma_{\text{sub(predicted)}} = 0.05 \text{ Mpc}^{-1}$  in the analysis presented in Section 5. The value for  $\Sigma_{\text{sub(predicted)}}$  used in the main analysis corresponds to a scenario in which disruption by the disk in our galaxy tidally disrupts halos twice as efficiently as the baryonic potential of a massive elliptical galaxy. However, our analysis does not depend on this choice, and we can repeat it with other values of  $\Sigma_{\text{sub(predicted)}}$ .

Figure C1 shows the inference of the power spectrum assuming  $\Sigma_{\text{sub(predicted)}} = 0.025 \text{ Mpc}^{-1}$ . As there are fewer total halos, the data places less stringent constraints on the mass-concentration relation, which in turn leads to slightly weaker constraints on the power spectrum.

#### APPENDIX D: COVARIANCE MATRICES OF POWER SPECTRUM AMPLITUDES

Our constraints on the power spectrum amplitude at different  $k$  scales are not independent since we assume an analytic model for the power spectrum. Using the results of this analysis to constrain a model for  $P(k)$  more than one  $k$  scale

therefore requires the covariance matrix between the samples at different scales. We obtain the covariance matrix for samples of the posterior distributions  $\tilde{p}(P_k | \mathbf{D})$

$$M = \begin{pmatrix} 0.10 & 0.16 & 0.21 \\ 0.16 & 0.27 & 0.37 \\ 0.21 & 0.37 & 0.53 \end{pmatrix}.$$

where the first, second, and third entries correspond to  $\log_{10} P(k)$  evaluated at  $k = 10, 25$ , and  $50 \text{ Mpc}^{-1}$ .